# Sequential, Low-Temperature Aqueous Synthesis of Ag-In-S/Zn Quantum Dots via Staged Cation Exchange under Biomineralization Conditions

**Sequential, Low-Temperature Aqueous Synthesis of Ag-In-S/Zn Quantum Dots via Staged Cation Exchange under Biomineralization Conditions**

Nur Koncuy Ozdemir[1], Joseph P. Cline[2], John Sakizadeh[1], Shannon M. Collins[1], Angela C. Brown[1], Steven McIntosh[1], Christopher J. Kiely[1,2], Mark A. Snyder[1*]

[1] Dept. of Chemical and Biomolecular Engineering, Lehigh University, Bethlehem, PA 18015,

United States

[2] Dept. of Materials Science and Engineering, Lehigh University, Bethlehem, PA 18015,

United States

* Corresponding author: snyder@lehigh.edu (M.A. Snyder)

**Keywords:** biomineralization, quantum dots, sequential synthesis, targeted bioimaging

## Abstract

The development of high quality, non-toxic (*i.e.*, heavy-metal-free), and functional quantum dots (QDs) via

'green' and scalable synthesis routes is critical for realizing truly sustainable QD-based solutions to diverse

technological challenges. Herein, we demonstrate the low-temperature all-aqueous-phase synthesis of silver

indium sulfide/zinc (AIS/Zn) QDs with a process initiated by the biomineralization of highly crystalline

indium sulfide nanocrystals, and followed by the sequential staging of $Ag^+$ cation exchange and $Zn^{2+}$

addition directly within the biomineralization media without any intermediate product purification. Therein,

we exploit solution phase cation concentration, the duration of incubation in the presence $In_2S_3$ precursor

nanocrystals, and the subsequent addition of $Zn^{2+}$ as facile handles under biomineralization conditions for

controlling QD composition, tuning optical properties, and improving the photoluminescence quantum

yield of the AIS/Zn product. We demonstrate how engineering biomineralization for the synthesis of

intrinsically hydrophilic and thus readily functionalizable AIS/Zn QDs with a quantum yield of 18% offers

a 'green' and non-toxic materials platform for targeted bioimaging in sensitive cellular systems. Ultimately,

the decoupling of synthetic steps helps unravel the complexities of ion exchange-based synthesis within the

biomineralization platform, enabling its adaptation for the sustainable synthesis of 'green', compositionally

diverse QDs.

## INTRODUCTION

Semiconductor nanocrystals (NCs) or quantum dots (QDs) offer unique optical and electronic properties as a result of quantum confinement effects, which can be exploited in applications as diverse as photocatalysis to bioimaging.[1–3] The photostability and quantum yield (QY), long lifetimes, and near-infrared (NIR) emission of QDs, coupled with the ability to functionalize them with multiple targeting ligands, makes them versatile alternatives to common fluorophores for use in bioimaging applications.[4–10] The broad efficacy of candidate QDs for imaging under physiological conditions, however, generally hinges upon how readily biocompatibility can be achieved while preserving optical properties, and how simply and robustly the native surface functionality can be tailored to endow the QDs with biospecificity in aqueous environments.

Cadmium and mercury-based QDs have garnered much attention due to their high quantum yield (QY), size-tunable optical properties, narrow emission spectra, and functionalizabilty.[11] However, their broad deployment in 'green' and/or sensitive applications like bioimaging is undercut, on the one hand, by their compositional toxicity, and, on the other hand, by challenges stemming from their high-temperature, organic-phase synthesis.[12–15] Even when composition is adapted toward a greener materials palette, high-temperature organometallic synthesis routes lead to hydrophobic QDs that require ligand exchange and/or particle encapsulation in order to functionalize and apply them in aqueous biological systems.[16–20] In addition to being a costly and multi-step endeavor, such additional processing can ultimately alter the specific QD surface chemistry and, thereby, its electronic and optical properties.[19,21] The promise of QDs for targeted bioimaging has motivated efforts aimed at identifying simple, sustainable (*i.e.*, low-temperature), all-aqueous synthesis routes to 'green' (*i.e.*, biocompatible) hydrophilic QDs that are amenable to direct functionalization.[18,22,23]

The search for non-toxic alternatives to II-VI QDs has expanded to ternary or quaternary compositional palettes.[18,24] This has been driven in part by the potential to exploit particle composition for tuning optical properties[24,25] rather than relying solely on controlling particle size, which is a particular challenge when trying to maintain a narrow size distribution while ensuring particle stability.[26] I-III-VI QDs

exhibit tunable spectroscopic properties spanning the UV to the NIR region, and have large Stokes shifts, long PL lifetimes, and low toxicities.[11,15] Among this promising class of metal chalcogenides, Ag-In-S (AIS) QDs have garnered considerable interest in bioimaging applications[6–8,15,27–31] since they are non-toxic and have a useful band gap and Bohr diameter (1.87 eV, 5.5 nm, respectively).[32] Addition of higher band gap materials (*e.g.*, ZnS) in the form of shell structures or through quaternary alloying, has been demonstrated to help boost the generally lower photoluminescence quantum yields (PL QY)[11] of I-III-VI materials relative to II-VI type QDs that derive from intrinsic differences in electron-hole pair-trapping defects.[11,14]

Numerous recent reports on aqueous room temperature synthesis of AIS and AIS/Zn QDs have included rapid (10 min) single-pot synthesis[33] or staged synthesis employing metal nitrate precursors.[15] These reports have marked a transition away from persistent hydrothermal,[34] solvothermal,[22,35,36] microwave assisted[27] and single precursor thermal decomposition approaches[37] toward more sustainable synthesis of 'green' hydrophilic QDs. Yet, poor PL QYs (<1%) tend to be reported for low-temperature aqueous routes[15,33,38] unless additional hydrothermal annealing or high-temperature processing is carried out, or toxic solutes (*e.g.*, hydrazine hydrate) are used.[39]

Biomineralization, the process whereby the synthesis of inorganic materials is catalyzed or directed by biological systems (*i.e.*, cells, enzymes, biomolecules),[40] has been demonstrated as a viable all-aqueous, low-temperature route to a range of QD compositions, even resulting in materials with optical properties that rival those of QDs synthesized under high-temperature, organic phase conditions.[41] Cellular synthetic routes, employing *E. coli* bacteria for endogenous $H_2S$ production in solutions of metal nitrate precursors, have led to successful synthesis of AIS QDs in particular. Yet, such cellular processes tend to introduce purification challenges owing to QD attachment to the cell membrane.[42] Alternatively, extracellular single enzyme-based biomineralization of size-tunable metal sulfide QDs (*e.g.*, CdS, ZnS, PbS, CuInS$_2$ and CuZnSnS$_4$) has been demonstrated through the continuous turnover of L-cysteine to reactive $HS^-$ by an engineered strain of *cystathionine γ-lyase* (CSE) in the presence of buffered solutions of metal salts.[43–49]

Such enzymatic systems offer the benefits of biological processing without facing the purification challenges of cell-based systems.

Precisely how to leverage single enzyme biomineralization for the broader synthesis of I-III-VI or even quaternary QDs, however, remains a complex question given the effects of the endogenously produced $H_2S$ on both the thermodynamics[50,51] and kinetics[51,52] of the process. Specifically, the challenge of balancing the reactivity and stability of various cationic precursors proves especially acute within aqueous buffered solutions at low temperatures. Such conditions are required to maintain the activity of the enzymatic processes that are critical for biomineralization.[50–55] Our previous work on a related system ($CuInS_2$ with Zn addition) offered narrowly focused proof of the possibility of integrating cation exchange and biomineralization.[46] However, critical quantitative insight required to fully unravel the complexity of the associated thermodynamics and kinetics has yet to be fully elucidated. This has limited the establishment of key design rules required for harnessing biomineralization and cation exchange for the sustainable synthesis of multi-component, green, and hydrophilic QDs.

In this study, we have investigated the sequential all-aqueous, low-temperature synthesis of AIS/Zn QDs with tunable optical properties from biomineralized $In_2S_3$ nanocrystals (NCs). We demonstrate how sequential synthesis within a biomineralization medium, in which the formation of precursor nanocrystals and subsequent cation exchange are staged without any intermediate purification, enables tunability of particle composition and optical properties. Such compositional and functional tunability is generally not possible by conventional one pot approaches (*i.e.*, all reagents combined at the start).[15,42,50–62] Specifically, we establish how aqueous-phase, low-temperature enzymatic (CSE) turnover of the amino acid L-cysteine yields sufficient endogenous $H_2S$ in buffered solutions of indium chloride for the nucleation of $In_2S_3$ nanocrystals. Cysteine simultaneously serves as a source of $H_2S$ and stabilizer of the $In_2S_3$ nanocrystals throughout the subsequent Ag nitrate-based cation exchange process, leading to AIS QDs within the buffered aqueous biomineralization solution. We demonstrate how the solution-phase metal precursor ratio (In/Ag) offers a facile parameter for directly tuning the non-stoichiometric composition of the AIS product, and, thereby, the photoluminescence quantum yield (PL QY). We further elucidate the kinetics of Ag

exchange and subsequent $Zn^{2+}$ addition under biomineralization conditions for improving PL lifetime and PL QY.

Ultimately, we exploit the optical properties and biocompatibility of the resulting AIS/Zn quantum dots for targeted bioimaging. We demonstrate this through QD conjugation with key antibodies capable of selectively targeting protein receptors uniquely expressed on THP-1 macrophage membranes. Here, the hydrophilicity of the water-synthesized AIS/Zn QDs enables direct QD functionalization upon facile buffer exchange. The intrinsic biocompatibility over relevant timescales and ease of functionalizing the AIS/Zn QDs with targeting antibodies consequently offer the possibility for their broader customization based on unique receptor-antibody combinations characteristic of other cellular systems. More generally, the critical insight into cation exchange under biomineralization conditions advances the versatility of single enzyme biomineralization as a basis for the broadly sustainable and potentially scalable[43] synthesis of various 'green', non-toxic multi-component metal sulfide semiconductor QDs for a wide range of applications.

## EXPERIMENTAL

### Single-enzyme biomineralization of In$_2$S$_3$ QDs

The single enzyme biomineralization of In$_2$S$_3$ QDs follows previous reports of metal sulfide QD biomineralization resulting from the turnover of L-cysteine to reactive $HS^-$ in buffered solutions of metal salts by purified engineered strains of *cystathionine $\gamma$-lyase* (CSE).[43–47] Specifically, In$_2$S$_3$ biomineralization was initiated from a solution of 2 mM indium chloride (InCl$_3$; Alfa Aesar, metals basis, 99.999%), 8 mM L-cysteine (Spectrum Chemicals), and 0.1 mg/ml CSE in a 0.1 M Tris-HCl (pH 9.0, VWR) buffer solution, incubated at 37 °C for up to 24 h under continuous 125 rpm agitation by a New Brunswick Scientific I26 Shaker. Inductively Coupled Plasma Optical Emission Spectroscopy (ICP-OES) was employed to quantify total In(III) concentration (nominally *ca.* 1.9 mM) on the basis of a nominal, purified and acid-digested In$_2$S$_3$ solution (details in SI). Cross-correlation with UV-vis absorbance measurements of the same solution established a means for quantifying the concentration of In(III), $C_{In(III)}$, on the basis of net absorbance

measured from the In$_2$S$_3$ solutions, $(A_{sample} - A_{buffer})$, at a wavelength of 300 nm in 1 cm pathlength cuvettes according to

$$C_{In(III)}\ (ppm) = \frac{A_{sample} - A_{buffer}}{0.066}, \ \ (Eq.\ 1)$$

where $A_{sample}$ and $A_{buffer}$ denote the absorbance of the biomineralized In$_2$S$_3$ solution and native buffer, respectively, and the factor of 0.066 Au/ppm is the experimentally-determined proportionality constant correlating net absorbance with the concentration of In(III).

**Sequential synthesis of AIS QDs under all-aqueous, biomineralization conditions**

Synthesis of AIS QDs was initiated from biomineralized In$_2$S$_3$ solutions (diluted to *ca*. 1.5 mM In(III)) dosed with fresh L-cysteine to a concentration of 8 mM. Subsequently, prescribed amounts of silver nitrate (AgNO$_3$; Sigma Aldrich, ACS reagent, >99%) were added to achieve In(III)-to-silver molar ratios of In/Ag~2, 5, 10, and 20. The solutions were incubated at 37 °C for periods of 1-3 days.

**Room temperature preparation of AIS/Zn particles**

As-prepared AIS QD solutions of In/Ag~5 that had been incubated at 37 °C for 3 days were dosed with L-cysteine to a concentration of 32 mM cysteine, under the assumption that all cysteine previously in the synthesis solution had been turned over by CSE or consumed by AIS QD capping. Sufficient zinc acetate (Zn(OaAc)$_2$; Alfa Aesar Puratronic, 99.995% metals basis) was subsequently introduced to achieve a molar solution composition of Zn/In~4. The solution was incubated on an orbital shaker for 30 min at room temperature, and the AIS/Zn product was cleaned by a dissolution-precipitation method (details given in SI).

**Characterization**

Absorbance measurements were carried out on a UV-vis 2600 Shimadzu spectrophotometer equipped with an ISR-2600-Plus integrating sphere attachment. Photoluminescence measurements were performed using a QuantaMaster 400 (Photon Technology International). PL QY was calculated based on a Rhodamine 101 reference dye with the excitation wavelength of 400 nm. PL lifetime measurements were obtained on a Fluorolog-3 spectrofluorometer with an attached Time-Correlated Single-Photon Counting

(TCSPC) controller using 287 nm excitation (Delta Diode laser) and 580 nm detection. Electron microscopy studies were carried out on QDs that were cleaned by dissolution-precipitation methods (details given in SI), re-suspended in deionized water (DI water), and then dispersed by drop casting on holey carbon film (HC400-Cu) transmission electron microscope (TEM) grids. Analysis was conducted on a JEOL ARM200CF scanning transmission electron microscope (STEM) operating at an accelerating voltage of 200 kV. To determine the particle size distribution (PSD) and polymorphic form, bright-field and high-angle annular dark field (HAADF) images were collected. Image filtering was conducted in DigitalMicrograph, and JEMS was used to simulate the crystal structures and diffraction patterns for different polymorphs of In-S, AIS, and AIS/Zn QDs.

## Cell viability studies

THP-1 cells (ATCC, Manassas, VA, USA) were cultured in RPMI 1640 medium (Thermo Fisher Scientific), supplemented with 10% fetal bovine serum (FBS; Quality Biological) and 0.05 mM 2-mercaptoethanol (VWR), at 37 °C under 5% $CO_2$ for 2 weeks. The media was refreshed every 2-3 days to maintain a cell density of $0.2-1.0 \times 10^6$ cells/ml.[63] The biocompatibility of the AIS/Zn QDs was assessed by incubating THP-1 monocytes (*ca.* $10^5$ cells/mL) in PBS buffer at 37 °C in the absence (PBS buffer only) and presence of 25 µM and 50 µM AIS/Zn QDs. Following 1 h and 24 h incubation, a Trypan blue dye exclusion assay was employed to stain dead cells, and cell viability was quantified with an Invitrogen Countess II Automated Cell Counter.

## Preparation of antibody-conjugated AIS/Zn QDs

The anti-CD11b antibody (H5A4) supernatant, developed by J.T. August and J.E.K. Hildreth of Johns Hopkins University, was obtained from the Developmental Studies Hybridoma Bank, created by the NICHD of the NIH and maintained at the University of Iowa, Department of Biology, Iowa City, IA 52242. Anti-CD11b-conjugated AIS/Zn QDs, referred to as CD11b-QD, were prepared by covalently conjugating anti-CD11b antibody (H5A4) to AIS/Zn QDs using EDC (1-ethyl-3-(3-dimethylaminopropyl) carbodiimide hydrochloride; Thermo Fisher Scientific) / NHS (N-hydroxysulfosuccinimide; Thermo Fisher

Scientific) chemistry. Specifically, as-synthesized AIS/Zn QD solutions were sterilized by passage through a 0.2 μm PES filter. The QDs in Tris-HCl buffer (pH 9) were then re-suspended in 1X phosphate-buffered saline (PBS; pH 7.4), followed by three washes in PBS using 30-kDa Amicon centrifugal filters (4500 g, 5 min). 500 μL of a 20 mg/mL EDC solution and 500 μL of a 20 mg/ml NHS solution were added to 5 ml of the sterilized AIS/Zn QDs in PBS solution, and the solution was incubated for 30 min at room temperature. Conjugation of the anti-CD11b antibody to AIS/Zn QDs was initiated by the addition of 50 μl of anti-CD11b antibody, followed by incubation for 30 min at room temperature.

**Selective AIS/Zn QD-based bioimaging of THP-1 macrophages**

THP-1 cells (monocytes) were differentiated into macrophages by first dosing 10 mL of the cell solution with phorbol-12-myristate-13-acetate (PMA; Sigma-Aldrich) to a concentration of 200 nM. Upon gentle mixing, 1 mL aliquots were added to ibiTreat μ-Dishes (ibidi; Martinsried, Germany) and incubated for 48 h at 37 °C under 5% $CO_2$. The cell media was then replaced with fresh RPMI media (without PMA), removing monocytes (non-adherent) and leaving behind macrophages (adherent), and incubated for an additional 24 h prior to confocal imaging.[64]

THP-1 monocytes were prepared for confocal imaging controls by addition of 1 mL of the monocyte suspensions to poly-L-lysine (PLL)-treated ibiTreat μ-Dishes. 30 min incubation at room temperature allowed for monocyte settling and adhesion to the PLL-treated substrate. All cells were fixed with 4% (w/v) paraformaldehyde (PFA; Sigma-Aldrich) in PBS for 15 min. After triple washing with PBS buffer, the cells were incubated with 1% (w/v) bovine serum albumin (BSA; Alfa-Aesar) in PBS for 1 h at room temperature to neutralize electrostatics of the cell membrane and, thereby, to minimize the potential for non-specific binding of QDs.[64] The separately plated monocytes and macrophages were incubated at 4ºC overnight in the presence of media containing i) neither QDs nor anti-CD11b (control), ii) anti-CD11b antibody, iii) unconjugated AIS/Zn QDs, and iv) anti-CD11b-conjugated AIS/Zn QDs. Prior to confocal imaging, all cells plated in μ-dishes were washed twice with PBS buffer to remove non-adherent components in the corresponding media. Confocal images were collected using a Nikon Eclipse Ti inverted

microscope employing a 10x air-immersion objective lens with numerical aperture (NA) of 1.2, for multi-channel fluorescence imaging at 405 nm, 488 nm, and 561 nm excitation wavelengths.

## RESULTS and DISCUSSION

The biomineralization of binary QDs can be accomplished by low-temperature enzymatic (CSE) turnover of L-cysteine to endogenous $H_2S$ in buffered aqueous solutions of metal salts.[43–47] Direct extension of this scalable[43], 'green', one-pot aqueous technique to the synthesis of ternary QDs requires compatible stability and reactivity of the various metal salt precursors under optimal enzymatic conditions (*i.e.*, pH~9, 37 °C). In the specific case of AIS, while the indium chloride precursor is resistant to hydrolysis at pH 8.0 or above,[65,66] silver nitrate converts to silver hydroxide and silver oxide under these conventional biomineralization conditions, as evidenced by the instantaneous and persistent solution turbidity (**Figure S1**).[67]

Silver ions can be stabilized at pH 9 through complexation with cysteine,[68] enabling reaction with endogenously produced $H_2S$ to form $Ag_2S$ in a translucent brown solution (**Figure S1**). Yet, the promise for tunable one-pot biomineralization of AIS QDs is confounded by the tenuous dependence of Ag stability on cysteine. This represents a particular challenge for biomineralization given the continuous depletion of cysteine available for $Ag^+$ stabilization by enzymatic turnover of cysteine and its complexation with ionic or nanoparticulate species. Such decrease in the cysteine-to-silver ratio eventually destabilizes the system, as shown by the onset of turbidity in **Figure S2**,[68] whereas introduction of excess cysteine leads to undesired substrate-induced inhibition of CSE activity, which is detrimental to biomineralization.[69] While seemingly less critical in high-temperature and/or organic syntheses of AIS,[22,34–37] the decoupling of the synthetic steps in low-temperature, aqueous biomineralization-based approaches is, therefore, important for choreographing the associated stability, reactivity, and kinetics of the multi-component system.

### Biomineralization of highly crystalline $In_2S_3$ QDs

Two possible nanocrystalline starting points for sequential synthesis of AIS include $Ag_2S$ or $In_2S_3$, with subsequent cation exchange of In or Ag, respectively. The poor water solubility of $Ag_2S$[15,56] and

challenges with incorporation of In(III) into the $Ag_2S$ structure, owing to the rapid aqueous conversion of In(III) to $In(OH)_3$,[66] juxtaposed with the abundant indium vacancies within $In_2S_3$,[27] make the latter a more attractive nanocrystalline template despite its conventionally low crystallinity under low-temperature, aqueous synthesis conditions.[15,56,70] Our group previously demonstrated the efficacy of indium sulfide clusters, obtained through biomineralization of indium nitrate at the lower pH 7.5, as a starting point for $CuInS_2$ QD synthesis[46]. However, only UV-visible absorbance was reported as an indication of the formation of indium sulfide clusters of diameters of <1 nm. The extent to which indium sulfide nanoparticles can be biomineralized and their crystallinity maximized under buffered aqueous conditions has never been elucidated despite the impact of the crystalline template quality on the optical properties of the subsequently ion exchanged materials.

**Scheme 1.** Depiction of all-aqueous, biomineralization-based synthesis of hydrophilic AIS/Zn QDs, their functionalization with antibodies (anti-CD11b), and their deployment for selective bioimaging of THP-1 macrophages through selective association with uniquely expressed membrane proteins (CD11b).
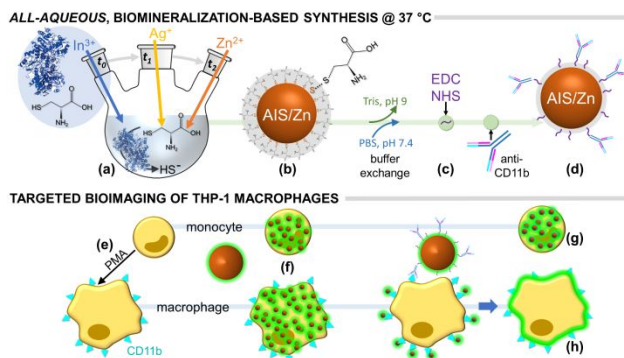


**(a)** Initial biomineralization **($t_0$)** of $In_2S_3$ QDs by the enzymatic turnover of L-cysteine to $HS^-$ in the presence of an $In^{3+}$ precursor, followed by sequential **($t_1$)** $Ag^+$ and **($t_2$)** $Zn^{2+}$ exchange under cysteine dosing, leads to **(b)** L-cysteine-capped AIS/Zn QDs. **(c)** Buffer exchange along with the addition of EDC/NHS reagents and CD11b antibody results in **(d)** anti-CD11b-conjugated AIS/Zn QDs. **(e)** CD11b receptors are uniquely expressed on the membranes of THP-1 macrophages such that **(f)** unconjugated QDs diffuse similarly into the THP-1 monocytes and macrophages, whereas anti-CD11b conjugated QDs **(g)** diffuse into monocytes, but **(h)** selectively conjugate to the CD11b expressed on the macrophage membrane.
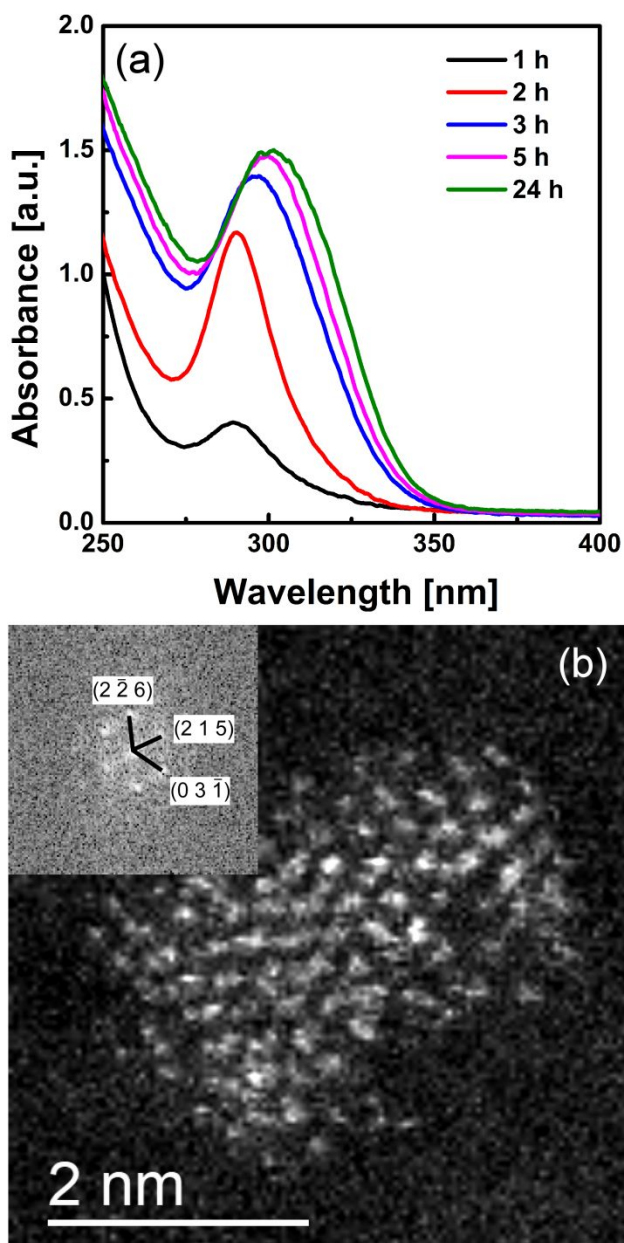
**Figure 1. (a)** UV-vis absorbance spectra as a function of incubation time and **(b)** a representative HAADF-STEM image and associated fast Fourier transform (FFT) of a resulting biomineralized $In_2S_3$ particle oriented along the $[8\bar{1}\bar{3}]$ zone axis, prepared by the incubation (37 ºC, 24 h) of solutions of 8 mM cysteine, 2 mM indium chloride, and 0.1 mg/ml CSE in Tris-HCl buffer (pH 9.0).

In order to seamlessly integrate biomineralization and cation exchange, we have explored the CSE-based turnover of L-cysteine in Tris-HCl buffered (pH 9.0) solutions of $InCl_3$ to prevent hydrolysis of the indium precursor and to facilitate cysteine-induced stabilization of Ag and Zn precursors during their staged introduction into the biomineralization solution (**Scheme 1a**).[65,66] **Figure 1a** tracks the UV-visible absorbance spectra of the synthesis solution at various time points over the course of 24 h incubation at 37

°C. A distinct absorbance band appears at 290 nm after 1 h incubation, similar to our prior reports, indicating the rapid biomineralization of sub-nanometer indium sulfide clusters. The evolution of the spectra over only the initial 5 h incubation period, namely the increase in intensity and red shift, is consistent with the estimated time for CSE-based turnover of approximately all free cysteine according to our earlier investigation of nominal CSE kinetics.[43] Tauc plot analysis estimates a corresponding band gap energy of the resulting indium sulfide particles of 3.8 eV, consistent with the formation of quantum confined $In_2S_3$ particles[71,72] given the 2.1-2.3 eV band gap reported for bulk $In_2S_3$.[25,73]

HAADF-STEM images and FFT of a representative particle in **Figure 1b** and image of a representative field of particles in **Figure S3a** show that the resulting materials are clearly crystalline. These data underscore the ability to biomineralize indium sulfide nanocrystals under ambient, aqueous buffered solutions. Particle size distribution measurements (**Figure S3b**), collected from images like the one shown in **Figure S3a**, indicate that the particles have a mean size of *ca.* 1.9±0.4 nm. While the complex unit cell of $In_2S_3$ (*i.e.*, tetragonal unit cell [I41/amd] containing 32 indium and 48 sulfur atoms, common vacancies, and irregular positions of indium atoms when viewed in projection) makes conclusive lattice indexing challenging, the interplanar angles and spacings (inset, **Figure 1b**; **Table S1**) are consistent with the formation of the tetragonal $In_2S_3$ polymorph. Moreover, XEDS analysis of the indium and sulfur content from a group of particles (**Figure S3c**) confirms a stoichiometric In:S ratio of *ca.* 1:1.5, consistent with the $In_2S_3$ polymorph.

An increase in intensity and red shift of absorbance is commonly interpreted to indicate respective growth of nanoparticle concentration and size. However, the known impact of the local chemical environment on absorbance, coupled with the high thiol-mediated affinity of cysteine for soft transition metal ions,[74] confounds such conventional interpretation in the biomineralized $In_2S_3$ system. Specifically, **Figure S4** shows how the addition of cysteine to an initially purified $In_2S_3$ solution leads to a decrease in absorbance intensity on a scale that is comparable to the changes observed during $In_2S_3$ biomineralization (**Figure 1a**).

Therefore, to minimize the confounding effects of cysteine on the quantitative characterization of the $In_2S_3$ system, all biomineralized $In_2S_3$ precursor solutions were incubated for 24 h—well in excess of the predicted 5 h needed for cysteine consumption—in order to ensure the complete enzymatic turnover of free cysteine before subsequent introduction of metal precursors for cation exchange. In addition, separate cross-correlation of the absorbance intensity with ICP-OES-based quantification of the In(III) concentration, enables standardization of In(III) concentration from sample to sample based simply on absorbance intensity of $In_2S_3$ solutions. This proves critical for quantitatively tailoring relative solution-phase metal cation ($Ag^+$, $Zn^{2+}$) concentrations in subsequent sequential cation exchange-based synthesis steps.

**Synthesis of $AgIn_5S_8$ (AIS) under low-temperature, buffered aqueous biomineralization conditions**

The addition of silver nitrate directly to the biomineralized $In_2S_3$ nanoparticle solution without any intermediate purification of the latter results in an instantaneous change from colorless to brown, followed by rapid (*i.e.*, within one minute) destabilization. This destabilization, indicated by the onset of solution turbidity, is attributed to the lack of free cysteine available for Ag complexation as a result of its enzymatic turnover during the biomineralization of $In_2S_3$ (**Figure S2**). Alternatively, dosing of the biomineralized $In_2S_3$ solution with cysteine prior to silver nitrate addition (**Scheme 1a ($t_1$)**) results in a brown translucent solution that remains stable for more than three days.

The 1-day incubation of solutions containing silver nitrate varying in In/Ag concentration ratio from ~2-20, leads to the measurement of distinct absorbance bands (**Figure 2a**) that are red-shifted by more than 50 nm relative to the band measured for the $In_2S_3$ QD precursor. The magnitude of this shift is attributed to successful $Ag^+$ incorporation into the $In_2S_3$ precursor particles. Moreover, Tauc plot analysis indicates a concomitant reduction in the band gap energy, relative to that measured for the $In_2S_3$ QD precursor, to below 3.2 eV (**Figure 2b**). This is consistent with the synthesis of AIS QDs, given that the reported band gap for bulk AIS is 1.87 eV.[32] It also explains the onset of the distinct PL emission for these

solutions (**Figure 2c**) under excitation wavelengths for which the biomineralized $In_2S_3$ NCs were not photoluminescent.

The distinctive absorbance and PL emission spectra, resulting from adjusting the In/Ag ratio in the biomineralization synthesis solutions, indicates a facile mode for tuning the $Ag^+$ incorporation within, and thus optical properties of, sequentially synthesized AIS QDs. Namely, increasing the In/Ag ratio results in a blue shift in both the absorbance onset (**Figure 2a**) and PL emission peak wavelength (**Figure 2c**) as well as a concomitant increase in the band gap energy (**Figure 2b**). Established here specifically for ambient buffered biomineralization systems, these trends in optical properties are consistent with literature reports on the variations in composition of AIS QDs.[34,36,75]
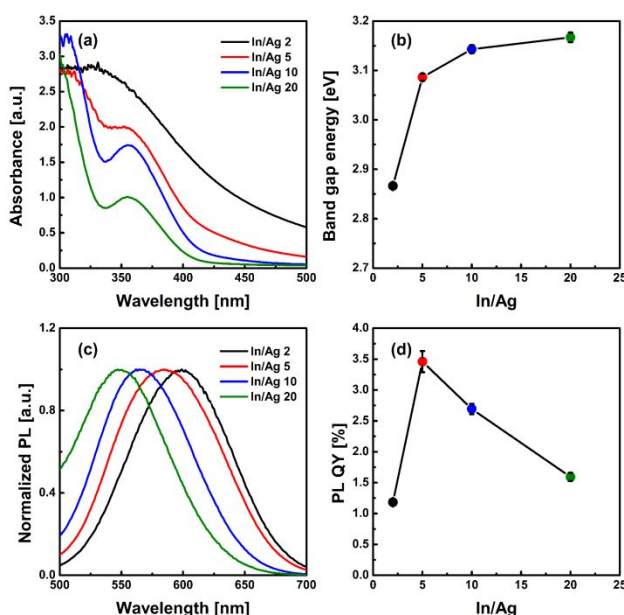


**Figure 2.** The effect of initial indium-to-silver molar ratio (In/Ag) on the **(a)** absorbance, **(b)** band gap energy, **(c)** PL emission (excitation wavelength 400 nm) spectra, and **(d)** PL QY of AIS particles sequentially synthesized by 1-day incubation (37 °C) of buffered (pH 9.0) solutions of biomineralized $In_2S_3$ NCs (1.5 mM In(III)) dosed with 8 mM cysteine in the presence of specified silver nitrate concentrations.

The PL QY trends nonmonotonically with increasing In/Ag ratio (**Figure 2d**), which is consistent with the literature reports that attribute the maximum in QY to composition-dependent variations of intrinsic defects.[76] The specific optimum In/Ag ratio of ~5, identified from among the compositions studied here, is in agreement with the corresponding literature-reported range for this maximum of In/Ag~1-9 (*i.e.*,

In/Ag~1,[77] 1.7,[78] 4,[15,34–36,72] 5,[79,80] 9[81]). The wide variation of reported In/Ag optima is likely a manifestation of differences in synthesis conditions such as temperature, capping ligand, and synthesis medium.[53,54]

Being able to fully exploit $Ag^+$ incorporation as a facile handle for tuning the optical properties of the synthesized AIS QDs requires quantification of the characteristic time scales for ion exchange specifically in the buffered aqueous, low-temperature biomineralization system. To do so, we have measured the optical properties of AIS nanocrystals synthesized via $Ag^+$ cation exchange with the biomineralized $In_2S_3$ particles during periods of incubation of up to 3 days. This extended time scale is dictated by the low-temperature conditions and thus slower exchange kinetics relative to hydrothermal processing, but restricted by stability limits resulting from dimerization-based depletion of the cysteine capping agent. **Figure 3** shows corresponding trends of the band gap energy, PL QY, and PL emission peak wavelength with increasing incubation time. Upon extended incubation, biomineralization solutions with In/Ag~5-20 remain stable. However, a brown precipitate forms at the highest concentration of Ag studied here (In/Ag~2), attributable to insufficient metal complexation and/or particle capping under these conditions.
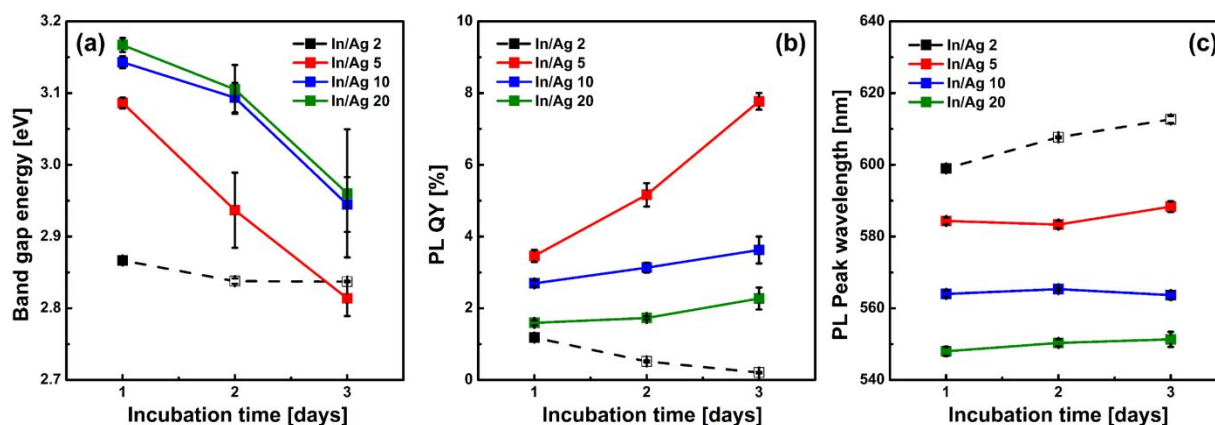


**Figure 3.** The effect of incubation times of 1-3 days on the **(a)** band gap energy, **(b)** PL QY, and **(c)** PL peak wavelength of AIS particles sequentially synthesized at 37 °C in buffered (pH~9) solutions of biomineralized $In_2S_3$ NCs (1.5 mM In(III)) dosed with 8 mM cysteine in the presence of specified silver nitrate concentrations. Stable and unstable solutions are differentiated by closed symbols/solid lines and open symbols/dashed lines, respectively.

Generally, the band gap energy decreases with increasing incubation time (**Figure 3a**). Whereas the magnitude and evolution of the band gap remains statistically comparable between the In/Ag~10 and

20 samples over the course of the 3-day incubation, the band gap is markedly smaller and decreases most significantly in the case of the In/Ag~5 sample. The PL QY (**Figure 3b**) increases with incubation time, similar to what has been shown in previous studies using alternative hydro/solvothermal synthesis approaches.[35,75,81] As with the band gap, the PL QY increases most significantly (*ca*. 125%) for the In/Ag~5 sample whereas the sensitivity of the In/Ag~10 and 20 samples to extended incubation is much weaker. These data underscore how even low-temperature incubation of the AIS particles within the buffered biomineralization solutions is able to improve PL QY to levels concomitant with common hydro/solvothermal synthesis of I-III-VI type QDs (*ca.* 10%).[11,14,82] Ultimately, the PL QY falls short of very recent reports of high-temperature and/or organic synthesis of AIS particles,[82,83] likely due to the higher defect concentrations intrinsic to the lower-temperature[82] aqueous[33] synthesis.
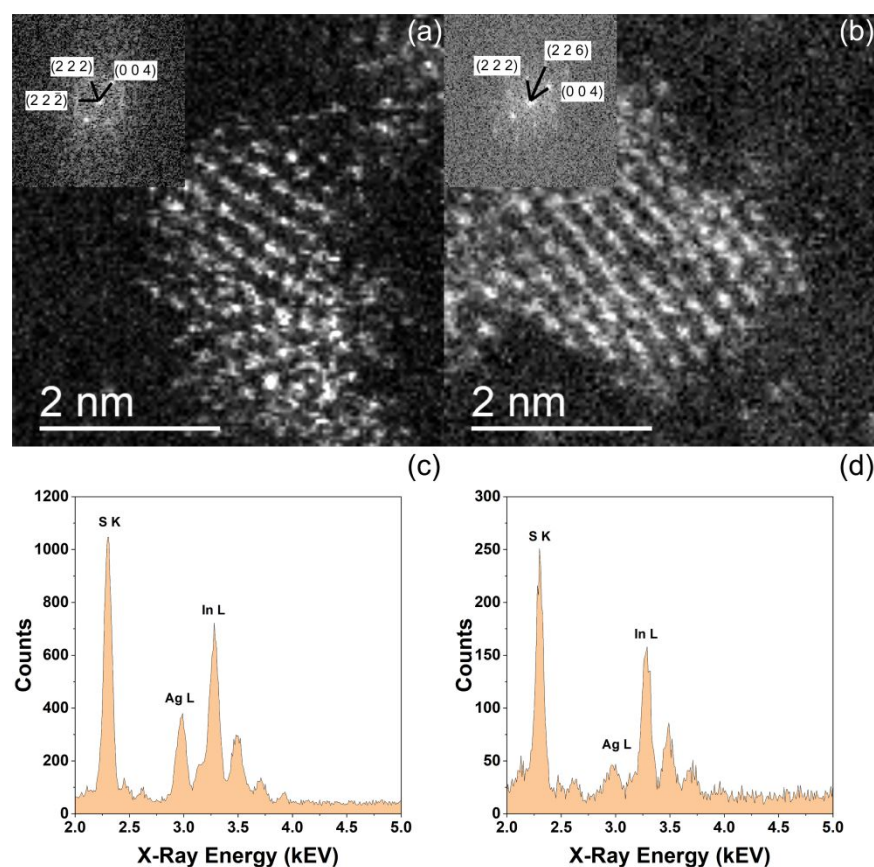


**Figure 4.** Representative HAADF-STEM images and associated FFT's (insets) of AIS particles resulting from incubating biomineralized $In_2S_3$ particles for 3 days in solutions with In/Ag molar ratios of **(a)** 5 and **(b)** 10, showing the common $[\bar{1}10]$ type zone axis for the cubic $AgIn_5S_8$ structure. Associated XEDS spectra are shown in **(c)** and **(d)**, respectively.

Electron microscopy of the AIS QDs offers first insight into the size and crystallinity of the incubation-evolved product and how particle composition correlates with the composition of the synthesis solutions. Representative HAADF-STEM images and associated FFTs of individual AIS nanocrystalline particles, synthesized by 3-day $Ag^+$ cation exchange (In/Ag~5 and 10) directly with biomineralized $In_2S_3$ precursor particles, are shown in **Figure 4a,b**. Representative lower magnification HAADF-STEM images of a field of particles from the In/Ag~5, 10 and 20 samples are shown in **Figure S5**. Indexing of the representative AIS particles leads to a good match of interplanar spacings and angles with the $AgIn_5S_8$ polymorph as quantified in **Table S2**. We do not observe the presence of any $Ag_2S$.

XEDS spectra for each particle composition, collected from particle populations like those shown in **Figure S5**, are included in **Figure 4c,d** and **Figure S6** for samples prepared from synthesis solutions with nominal compositions of In/Ag~5 and 10 and In/Ag~20, respectively. XEDS analysis detects the presence of both indium and silver in all samples. The elemental composition of the synthesized particles closely tracks the nominal In/Ag concentrations within the synthesis solution (**Figure 4c,d, Figure S6, Table 1**). While the XEDS measurements are semi-quantitative, they are sufficiently accurate to confirm that the exact stoichiometry of $AgIn_5S_8$ is not achieved, suggesting that the final crystalline particles contain vacancies and that $Ag^+$ is partially exchanged with $In^{3+}$ and undergoes incomplete vacancy incorporation over the course of the 3-day incubation.

**Table 1.** Particle size distribution (PSD) and XEDS elemental analysis as a function of the molar In/Ag solution ratio for biomineralized $In_2S_3$, AIS, and Zn-incorporated AIS/Zn QDs.

| Sample | PSD Average [nm] | EDS In/Ag (solid) | Nominal In/Ag (solution) |
|---|---|---|---|
| $In_2S_3$ | 1.9±0.4 | - | - |
| In/Ag 5 | 1.9±0.3 | 4.2 | 5 |
| In/Ag 10 | 1.9±0.4 | 10.9 | 10 |
| In/Ag 20 | 1.7±0.4 | 15.2 | 20 |
| AIS/Zn | 2.1±0.4 | 5.3 | 5 |

AIS particle size distributions (PSDs) (**Figure S5**) were collected from the measurement of populations of *ca*. 100 or more crystalline particles on the basis of HAADF-STEM images. The size of AIS

particles (**Table 1**) of varying nominal In/Ag ratio are statistically indistinguishable from one another as well as from the $In_2S_3$ precursor particles. Therefore, the blue shift in PL peak wavelength with increasing In/Ag ratio (**Figure 3c**) appears to derive from the particle composition rather than particle size. The latter apparently also plays little role in the evolution of other optical properties upon incubation. Moreover, the modest polydispersity (*ca.* 20%) of all AIS particles suggests that the broad full width at half maximum (FWHM) of the associated PL bands (**Figure 2c**, **Figure S7**) is not indicative of a wide size distribution. Instead, it is attributable to defect-based donor-acceptor pair recombination of photogenerated charge carriers via defect sites, consistent with existing literature.[35,84]

Ruling out particle size as a contributing factor, the observed evolution of optical properties with increasing incubation time could instead be a manifestation of one of a number of possible factors, including i) defect reduction and/or ii) continuation of the host ($In^{3+}$)-guest ($Ag^+$) cation exchange process.[15,56] The more marked changes in optical properties for the In/Ag~5 sample likely stem from the higher relative $Ag^+$ concentration and thus highest driving force for cation exchange among the stable solution conditions studied. The relative insensitivity of the PL peak wavelength to extended incubation (**Figure 3c**), however, suggests that the changes with incubation are likely not dominated by a significant increase in $Ag^+$ exchange over the course of the extended incubation.[35,75,81] Rather, they are more likely due to effective low-temperature annealing of the particle structure as well as evolving surface passivation.[15,66,75]

In order to gain insight into potential structural evolution during incubation as well as the role of $Ag^+$ exchange in tuning optical properties of the AIS particles under biomineralization conditions, we have employed time correlated single photon counting measurements[85] to characterize In/Ag~5 samples incubated for time periods of 1 to 3 days. We have also drawn comparisons with the 3-day In/Ag~10 and 20 samples. The time resolved photoluminescence decay for corresponding AIS QDs incubated at 37 ºC for 1 day (AIS-1d) to 3 days (AIS-3d) are shown in **Figure 5a**. The parameters associated with the biexponential fits are listed in **Table S3**. The resulting average PL lifetime, $\tau_{avg}$, increases by more than 40% to *ca.* 50 ns upon incubation for 3 days. At the same time, the contribution of the fast decay component, $B_1$, decreases by more than 65% (**Figure 5b**). $B_1$ indicates contributions of intrinsic recombination

processes of initially populated core states with surface defects, such as dangling bonds and vacancies.[65,80,86]

Therefore, these data suggest that structural annealing and/or healing of surface defects during low-temperature incubation[66,75,76] are responsible, at least in part, for the observed QY enhancement with incubation under biomineralization conditions (**Figure 3b**).
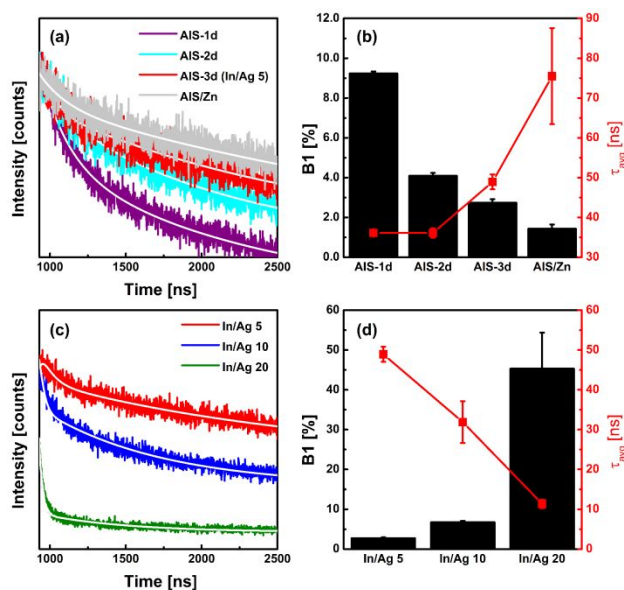


**Figure 5.** The effect of 1-day (1d), 2-day (2d), and 3-day (3d) incubation on **(a)** the time resolved photoluminescence decay of AIS (In/Ag~5) and AIS/Zn QDs and **(b)** the contribution of the fast decay component, B1, and average PL lifetime, $\tau_{avg}$. The effect of In/Ag ratio on **(c)** the time resolved photoluminescence decay of AIS QDs prepared by 3-day incubation and **(d)** the contribution of the fast decay component, B1, and average PL lifetime, $\tau_{avg}$.

The photoluminescence decay curves and associated biexponential fits (parameters in **Table S3**) for AIS samples of varying In/Ag ratios incubated for 3 days are compared in **Figure 5c**. The average PL lifetime, $\tau_{avg}$, increases with decreasing In/Ag ratio as a result of a corresponding decrease in the fast surface defect-mediated decay ($B_1$) in favor of slower, radiative donor-acceptor recombination ($B_2$) (**Figure 5d**).[65,80,86] Persistent defects, originating more likely from the intrinsically faster rates of growth in the absence of coordinating solvents (e.g., TOPO[87]) than to the specific buffered biomineralization conditions, translate to average PL lifetimes that are approximately six times lower than hydro/solvo-thermally synthesized AIS QDs.[34,36] However, this deconvolution of the dominant recombination pathways points to the potential to mitigate the impact of the fast decay components by further increasing $Ag^+$ cation exchange in order to extend the average PL lifetime of the AIS QDs discussed herein.

**Low-temperature, aqueous addition of $Zn^{2+}$ to AIS QD system**

Given the stability limits on the Ag precursor in the buffered aqueous biomineralization system (**Figure S2**) and limits on the total $Ag^+$ exchange, the identification of additional biomineralization-compatible means for reducing the number and or severity of surface defects in order to fully maximize the PL QY are especially important since the PL QY of I-III-VI type QDs is known to be inherently lower than that for II-VI QDs.[82,88] To this end, we have separately leveraged Zn for its wide band gap, low toxicity, and demonstrated ability to passivate surface defects while simultaneously protecting against photodegradation.[89]

$Zn^{2+}$ stability under the buffered biomineralization conditions requires careful control and exploitation of cysteine complexation to ensure stability of the system during zinc addition. Specifically, the addition of Zn acetate precursor directly to the AIS solution results in rapid precipitation, owing to $Zn^{2+}$ complexation with, and destabilization of, the CSE enzyme. In order to stabilize the $Zn^{2+}$ cations against such deleterious enzyme complexation, it is necessary to replenish cysteine prior to the introduction of the zinc precursor. This must be done in order to offset the loss of cysteine occurring during $Ag^+$ exchange as a result of its turnover by any persistently active CSE and its dimerization to form cystine.[43] Screening of cysteine dosing concentrations (4-32 mM) revealed the need to dose cysteine at a concentration of 32 mM prior to introduction of the zinc acetate precursor (**Scheme 1a ($t_2$)**) in order for the biomineralization solutions of In/Ag~5 AIS QDs to remain stable over the course of the 30 min incubation employed for $Zn^{2+}$ addition. Quantitative interpretation of the stabilization mechanism resulting from the concomitant molar ratio of Cys/Zn~5 is complicated by the numerous complexes that $Zn^{2+}$ forms under biomineralization conditions. These include complexes of $Zn^{2+}$ with CSE and cysteine, as well as the complexation of cysteine with the AIS particles.

Nonetheless, while the absorbance spectrum of the resulting particles appears unaffected by $Zn^{2+}$ addition (**Figure 6a**; **Scheme 1b**), the PL emission undergoes a slight blue shift relative to the native AIS particles (**Figure 6b**). Ultimately, the introduction of $Zn^{2+}$ more than doubles the PL QY to *ca.* 18% relative to the base In/Ag~5 AIS QDs (inset, **Figure 6a**). This can be attributed to the surface passivation, consistent

with earlier literature reports,[15,90,91] as evidenced by time correlated single photon counting (**Figures 5a,b**, **Table S3**). Namely, that analysis shows a decrease in the contribution of the fast decay component, $B_1$, and marked (*ca*. 50%) increase in the average PL lifetime upon $Zn^{2+}$ addition (AIS/Zn).
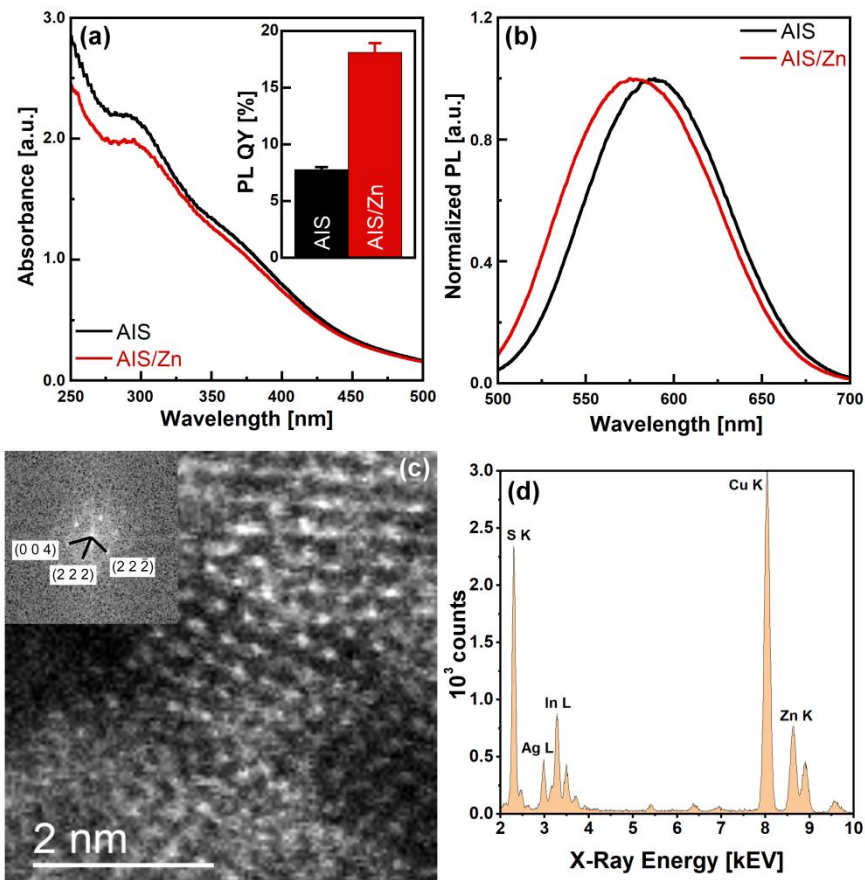


**Figure 6.** Sensitivity of **(a)** absorbance and PL quantum yield (inset) as well as **(b)** PL emission spectra to low-temperature $Zn^{2+}$ addition into AIS particles. **(c)** HAADF-STEM image and corresponding FFT from a representative AIS/Zn QD, oriented along the $[\bar{1}10]$ zone axis of the cubic $AgIn_5S_8$ structure, with **(d)** XEDS data indicating successful Zn addition.

A representative HAADF-STEM image of the resulting AIS/Zn particles is shown in **Figure 6c**, and representative images along several different zone axes are included in **Figure S8**. The associated indexing remains consistent with cubic $AgIn_5S_8$ (**Table S4**). The corresponding particle size distribution (**Figure S9b**), collected from images like the one in **Figure S9a**, shows a subtle increase in the average particle size (2.1±0.4 nm) relative to that of the AIS (In/Ag~5) precursor particles (**Table 1**). The corresponding XEDS spectrum (**Figure 6d**) confirms zinc addition, with an In/Zn atomic % ratio of 2.

Moreover, the increase in the In/Ag ratio upon zinc addition points to at least partial exchange of $Zn^{2+}$ and $Ag^+$.

Elemental mapping (**Figure S10**) indicates the apparent uniform, co-located distribution of In and Zn. Yet, the spatial resolution of XEDS mapping, coupled with the sparse distribution of low concentrations of the lighter element, zinc, in a matrix of heavier cations (Ag, In), confounds conclusive visualization of zinc localization via high angle dark field imaging. While the small characteristic diffusion length scale of the *ca.* 2 nm particles means that even limited cation diffusion under the low-temperature biomineralization conditions studied here makes Zn diffusion and formation of alloyed Ag-In-Zn-S possible,[15,89] literature reports[15] have highlighted how limited Frenkel pairs stymie $Zn^{2+}$ intercalation into AIS particles under room temperature conditions. Indeed, our measurement of similar band gaps for the native and Zn-incorporated AIS QDs (*i.e.*, both *ca.* 2.84±0.01 eV) suggests that Zn likely deposits primarily on the particle surface under the low-temperature biomineralization conditions studied here.

**Physiological stability and biocompatibility of biomineralization-derived AIS/Zn QDs**

As a result of the all-aqueous synthesis, the only key processing steps required for the eventual functionalization of the AIS/Zn QDs (**Scheme 1b**) and their deployment for targeted bioimaging is sterilization by filtration and facile aqueous exchange from the Tris-HCl (pH 9) synthesis buffer to phosphate-buffered saline (PBS; pH 7.4). The exchange into PBS was due to the suitability of this buffer for mimicking physiological conditions (**Scheme 1c**). Whereas the Tris-HCl (pH 9) buffer was critical for ensuring metal precursor stability during the staged cation exchange under biomineralization conditions, the synthesized AIS/Zn QDs do not suffer from equivalent stability issues upon transfer to the pH 7.4 PBS buffer. This is confirmed by time-dependent UV-vis absorbance and PL emission measurements of the AIS/Zn QDs after exchange into the PBS (pH 7.4) buffer (**Figure 7a,b**). Specifically, the insensitivity of the absorbance spectra and PL emission for incubation of the AIS/Zn particles for up to one week in the PBS buffer underscores their stability under physiological pH. Such extended stability is critical for the viability of the AIS/Zn QDs in bioimaging applications.
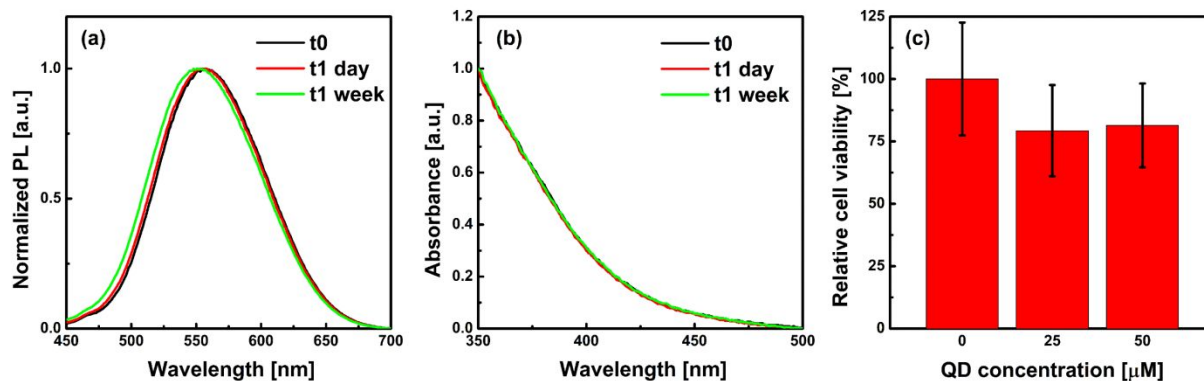
**Figure 7.** Stability of the AIS/Zn QDs following exchange into PBS (pH 7.4) buffer assessed by **(a)** absorbance and **(b)** photoluminescence before ('t0') and after incubation for 1 day ('t1 day') and 1 week ('t1 week') at 4 °C. **(c)** Cell viability assessment via Trypan blue dye exclusion assay after 24 h incubation of monocytes in the presence of variable concentration of AIS/Zn QDs. All data are normalized to untreated cells. Each data point represents the mean (n=3) $\pm$ standard deviation.

We have also evaluated the biocompatibility of the synthesized AIS/Zn QDs with the THP-1 cellular system, a human leukemia monocytic cell line. We assessed AIS/Zn QD-induced toxicity in the case of THP-1 monocytes using the conventional Trypan blue assay[92] (*i.e.*, percentage of living cells based on dye exclusion). QD toxicity depends on multiple factors such as QD size, concentration, capping ligands, coating material, and the time for which cells are incubated in the presence of QDs.[13,93] Cell viability remained at nearly 100% for short-time (1 h) incubation of THP-1 monocytes with AIS/Zn QDs at concentrations of *ca.* 25 μM (not shown). Upon extended (24 h) incubation of THP-1 monocytes in the presence of the same and even double the relatively high (μM) QD concentrations of AIS/Zn QDs, only a modest *ca.* 25% decrease in cell viability was observed (**Figure 7c**).[93,94] This highlights the apparent biocompatibility of the AIS/Zn QDs synthesized via the sequential, low-temperature biomineralization-initiated process described herein, underscoring their potential for live cell imaging especially at more common nM concentrations and shorter incubation times.

**Functionalization of biomineralization-based AIS/Zn QDs for targeted bioimaging**

The THP-1 cellular system has been widely used as an *in vitro* model of human macrophages differentiated from bone marrow-derived monocytes in response to infection or inflammation. Hence,

selective immunofluorescence staining of THP-1 macrophages over monocytes serves as an important

biological assay for gaining mechanistic insights into the associated infection/inflammation-induced

differentiation and the various roles of human monocyte-derived macrophages in other biological

processes.[95,96] The differentiation is accompanied by the expression of the CD11b receptor, a glycoprotein

in the $\beta_2$-integrin family of adhesion molecules, on the macrophage membrane. As such, CD11b offers a

unique protein signature for the targeted bioimaging of THP-1 derived macrophages.

Here, we have tested the efficacy of AIS/Zn QDs for immunofluorescence staining of these

macrophage-specific CD11b receptors by leveraging the hydrophilic character and native functionality of

the as-synthesized AIS/Zn QDs for conjugation with a CD11b antibody (anti-CD11b). Namely, cysteine,

the source of reactive $HS^-$ for enzymatic biomineralization of the $In_2S_3$ cores, caps the AIS/Zn QDs

through dative thiol bonding between its sulfur atom and the sulfur atoms on the QD surface (**Scheme 1b**).

The cysteine capping is preserved upon exchange from the synthesis buffer to PBS. This step eliminates

primary amines, belonging to the Tris synthesis buffer, so that the widely used and highly efficient and

stable EDC/NHS bioconjugation strategy (**Scheme 1c**) can be employed to successfully conjugate anti-

CD11b to the AIS/Zn QDs through the amine groups of the capping cysteines (**Scheme 1d**).

**Targeted bioimaging of THP-1 macrophage membranes by antibody-conjugated AIS/Zn QDs**

To test the labeling specificity achievable with the anti-CD11b-conjugated AIS/Zn QDs, we first

employed PMA to induce differentiation of THP-1 monocytes into macrophages (**Scheme 1e**).

Fluorescence confocal and merged images (fluorescence + bright-field) of the monocytes and macrophages

are shown as the 'control' samples in **Figure 8a**. The distinct size difference observed for the 'control' cells

is consistent with the reported difference in size between macrophages (*ca*. 20-30 μm) and monocytes (*ca*.

7-9 μm),[97,98] indicating the successful monocyte-to-macrophage differentiation of the THP-1 cells. The

absence of fluorescence signal for these 'control' monocytes and macrophages, where neither anti-CD11b

nor anti-CD11b-conjugated QDs have been added to the system, indicates negligible autofluorescence

under the imaging conditions employed herein. Similarly, even when the monocytes and macrophages were

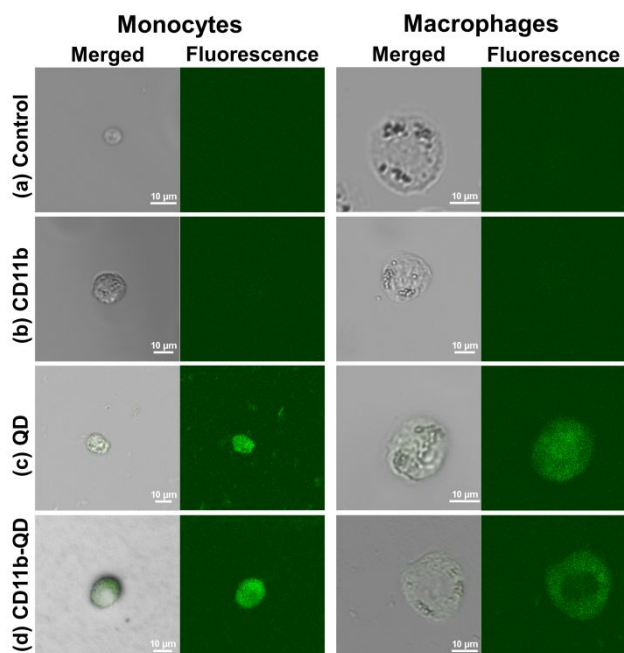incubated with just the antibody (anti-CD11b), negligible autofluorescence was again observed (**Figure 8b**).



**Figure 8.** Representative fluorescence and merged fluorescence + bright-field optical images of THP-1 monocytes (left double column) and macrophages (right double column) incubated in the presence of **a)** neither antibody nor QDs ('control'), **b)** anti-CD11b antibody ('CD11b'), **c)** native AIS/Zn QDs ('QD'), or **d)** AIS/Zn QDs conjugated with anti-CD11b antibody ('CD11b-QD').

Distinct fluorescence is, however, observed in the cases where the monocytes and macrophages have been incubated in the presence of native AIS/Zn QDs ('QD', **Figure 8c, Scheme 1f**). These QDs are the nominal buffer-exchanged product of the aqueous, biomineralization-based synthesis, bearing cysteine capping ligands but no CD11b-targeting antibody (**Scheme 1b**). The spatially uniform fluorescence of both the monocytes and macrophages under these conditions points to the unfettered penetration of the membranes of both cell types by the unconjugated photoluminescent QDs.

Upon attaching the anti-CD11b antibody to the AIS/Zn QDs (**Scheme 1d**) and incubating monocytes with the conjugated product, spatially uniform fluorescence is again observed (**Figure 8d**, **Scheme 1g**). This insensitivity of monocytes to anti-CD11b-conjugation of the QDs is consistent with negligible CD11b expression on the monocyte membrane, and thus lack of specific targets for the labeled QDs. When the same anti-CD11b-conjugated AIS/Zn QDs are incubated with the macrophages, however,

imaging of the cells reveals a distinct fluorescent ring and non-fluorescent core, as corroborated by the representative 2D optical slice of a representative field of fluorescence-ringed macrophages (**Figure S11**). The distinct ringed fluorescence in the case of the macrophages clearly indicates the success of the anti-CD11b-conjugated AIS/Zn QDs to selectively target CD11b receptors expressed on the macrophage cell membrane (**Scheme 1h**).[95] These data underscore the potential of the CD11b-QDs for use in specific immunofluorescence staining of THP-1 macrophages. The CD11b-AIS/Zn QD construct explored here also has potential for broader application in bioimaging given the fact that CD11b is a common integrin receptor expressed on a host of other cells (*e.g.*, neutrophils, peritoneal B-1 cells, CD8+dedritic cells, CD8+ T cells).[99] More broadly, the ease of functionalizing the hydrophilic AIS/Zn QDs with any type of antibody should offer a powerful, all-aqueous, low-temperature QD platform for the targeting of many different cell types.

**CONCLUSIONS**

This study demonstrates the efficacy of low-temperature, all-aqueous-phase synthesis of hydrophilic, functionalizable AIS/Zn QDs under biomineralization conditions. The sequentially staged, bottom-up formulation, exploits the highly crystalline, biomineralized $In_2S_3$ nanoparticles for subsequent direct exchange and addition of select metal cations ($Ag^+$, $Zn^{2+}$) without any intermediate purification. The biomineralization and cation exchange steps were simply decoupled through staged precursor addition following the completion of $In_2S_3$ biomineralization. This staged synthesis helps circumvent challenges with disparate metal precursor kinetics and stabilities that confound conventional one-pot processing. Such challenges are especially acute under buffered aqueous, low-temperature biomineralization conditions, which we have employed here in an effort to directly synthesize hydrophilic multi-component QDs via a process that aligns with standards of 'green' and sustainable processing. The result is a systematic approach that allows for the kinetics and thermodynamics of low-temperature ion exchange to be harnessed, along with defect annealing under near-ambient biomineralization conditions, for tailoring non-stoichiometric QD composition. By doing so, we demonstrate the ability to tune optical properties of the multi-component

QDs without the need for changing particle size. The resulting hydrophilic, biocompatible QDs can be readily functionalized with appropriate antibodies without the need for costly ligand exchange and purification for targeted bioimaging.  Ultimately, the tunability of the optical properties of the readily functionalized QDs by a combination of choreographed cation exchange and defect annealing, establishes a sustainable, all-aqueous and low-temperature platform for synthesizing compositionally diverse QDs that requires only the identification of a suitable, biomineralizable template nanocrystal that is amenable to subsequent ion exchange.

## CONFLICTS OF INTEREST

There are no conflicts to declare.

**Supporting Information** ICP-OES analysis method, precipitation-dissolution cleaning procedure, $AgNO_3$ precursor stability assay, $In_2S_3$ HAADF-STEM images and associated analysis (PSD, XEDS), indexing of tetragonal $In_2S_3$, cysteine sensitivity of $In_2S_3$ absorbance, HAADF-STEM images of AIS (In/Ag~5, 10, 20) and associated analysis (PSD), XEDS spectrum for AIS particles (In/Ag~20), indexing of cubic $AgIn_5S_8$ (In/Ag~5, 10), PL FWHM of AIS particles as a function of incubation time and In/Ag, parameterization of biexponential fits of photoluminescence decay for AIS and AIS/Zn samples, supplemental HAADF-STEM images of AIS/Zn samples, indexing of AIS/Zn samples, HAADF-STEM image of field of AIS/Zn particles

along with associated analysis (PSD), XEDS elemental mapping (Zn, In, Ag) of AIS/Zn particles, 2D confocal optical slice of THP-1 macrophages incubated with anti-CD11b-conjugated AIS/Zn QDs.

## REFERENCES

(1)     Tsuji, I.; Kato, H.; Kobayashi, H.; Kudo, A. Photocatalytic $H_2$ Evolution Reaction from Aqueous Solutions over Band Structure-Controlled $(AgIn)_xZn_{2(1-x)}S_2$ Solid Solution Photocatalysts with Visible-Light Response and Their Surface Nanostructures. *J. Am. Chem. Soc.* **2004**, *126* (41), 13406–13413. DOI:10.1021/ja048296m.

(2)     Bera, D.; Qian, L.; Tseng, T.-K. K.; Holloway, P. H. Quantum Dots and Their Multimodal Applications: A Review. *Materials* **2010**, *3* (4), 2260–2345. DOI:10.3390/ma3042260.

(3)     Jamieson, T.; Bakhshi, R.; Petrova, D.; Pocock, R.; Imani, M.; Seifalian, A. M. Biological Applications of Quantum Dots. *Biomaterials* **2007**, *28* (31), 4717–4732. DOI:10.1016/j.biomaterials.2007.07.014.

(4)     Medintz, I. L.; Uyeda, H. T.; Goldman, E. R.; Mattoussi, H. Quantum Dot Bioconjugates for Imaging, Labelling and Sensing. *Nat. Mater.* **2005**, *4* (6), 435–446. DOI:10.1038/nmat1390.

(5)     Biju, V.; Itoh, T.; Ishikawa, M. Delivering Quantum Dots to Cells: Bioconjugated Quantum Dots for Targeted and Nonspecific Extracellular and Intracellular Imaging. *Chem. Soc. Rev.* **2010**, *39* (8), 3031–3056. DOI:10.1039/B926512K.

(6)     Song, J.; Jiang, T.; Guo, T.; Liu, L.; Wang, H.; Xia, T.; Zhang, W.; Ye, X.; Yang, M.; Zhu, L.; Xia, R.; Xu, X. Facile Synthesis of Water-Soluble Zn-Doped AgIn5S8/ZnS Core/Shell Fluorescent Nanocrystals and Their Biological Application. *Inorg. Chem.* **2015**, *54* (4), 1627–1633. DOI:10.1021/ic502600u.

(7)     Xuan, T.-T.; Liu, J.-Q.; Yu, C.-Y.; Xie, R.-J.; Li, H.-L. Facile Synthesis of Cadmium-Free Zn-In-S:Ag/ZnS Nanocrystals for Bio-Imaging. *Sci. Rep.* **2016**, *6* (1), 24459. DOI:10.1038/srep24459.

(8)     Jiao, M.; Li, Y.; Jia, Y.; Li, C.; Bian, H.; Gao, L.; Cai, P.; Luo, X. Strongly Emitting and Long-Lived Silver Indium Sulfide Quantum Dots for Bioimaging: Insight into Co-Ligand Effect on

Enhanced Photoluminescence. *J. Colloid Interface Sci.* **2020**, *565*, 35–42. DOI:10.1016/j.jcis.2020.01.006.

(9)     Foubert, A.; Beloglazova, N. V; Rajkovic, A.; Sas, B.; Madder, A.; Goryacheva, I. Y.; De Saeger, S. Bioconjugation of Quantum Dots: Review & Impact on Future Application. *TrAC Trends Anal. Chem.* **2016**, *83*, 31–48. DOI:10.1016/j.trac.2016.07.008.

(10)    Pathak, S.; Davidson, M. C.; Silva, G. A. Characterization of the Functional Binding Properties of Antibody Conjugated Quantum Dots. *Nano Lett.* **2007**, *7* (7), 1839–1845. DOI:10.1021/nl062706i.

(11)    Hamanaka, Y.; Ogawa, T.; Tsuzuki, M.; Kuzuya, T. Photoluminescence Properties and Its Origin of AgInS$_2$ Quantum Dots with Chalcopyrite Structure. *J. Phys. Chem. C* **2011**, *115* (5), 1786–1792. DOI:10.1021/jp110409q.

(12)    Anastas, P. T.; Zimmerman, J. B. Design Through the 12 Principles of Green Engineering. *Environ. Sci. Technol.* **2003**, *37* (5), 94A-101A. DOI:10.1021/es032373g.

(13)    Ron, H. A Toxicologic Review of Quantum Dots: Toxicity Depends on Physicochemical and Environmental Factors. *Environ. Health Perspect.* **2006**, *114* (2), 165–172. DOI:10.1289/ehp.8284.

(14)    Zang, Z.; Zeng, X.; Wang, M.; Hu, W.; Liu, C.; Tang, X. Tunable Photoluminescence of Water-Soluble AgInZnS–Graphene Oxide (GO) Nanocomposites and Their Application in-Vivo Bioimaging. *Sensors Actuators, B Chem.* **2017**, *252*, 1179–1186. DOI:10.1016/j.snb.2017.07.144.

(15)    Song, J.; Ma, C.; Zhang, W.; Li, X.; Zhang, W.; Wu, R.; Cheng, X.; Ali, A.; Yang, M.; Zhu, L.; Xia, R.; Xu, X. Bandgap and Structure Engineering via Cation Exchange: From Binary Ag$_2$S to Ternary AgInS$_2$, Quaternary AgZnInS Alloy and AgZnInS/ZnS Core/Shell Fluorescent Nanocrystals for Bioimaging. *ACS Appl. Mater. Interfaces* **2016**, *8* (37), 24826–24836. DOI:10.1021/acsami.6b07768.

(16)    Jin, S.; Hu, Y.; Gu, Z.; Liu, L.; Wu, H.-C. Application of Quantum Dots in Biological Imaging. *J. Nanomater.* **2011**, *2011*, 834139. DOI:10.1155/2011/834139.

(17)    Sharma, P.; Brown, S.; Walter, G.; Santra, S.; Moudgil, B. Nanoparticles for Bioimaging. *Adv. Colloid Interface Sci.* **2006**, *123–126*, 471–485. DOI:10.1016/j.cis.2006.05.026.

(18)    Martynenko, I. V; Litvin, A. P.; Purcell-Milton, F.; Baranov, A. V; Fedorov, A. V; Gun'ko, Y. K. Application of Semiconductor Quantum Dots in Bioimaging and Biosensing. *J. Mater. Chem. B* **2017**, *5* (33), 6701–6727. DOI:10.1039/C7TB01425B.

(19)    Zhou, J.; Liu, Y.; Tang, J.; Tang, W. Surface Ligands Engineering of Semiconductor Quantum Dots for Chemosensory and Biological Applications. *Mater. Today* **2017**, *20* (7), 360–376. DOI:10.1016/j.mattod.2017.02.006.

(20)    McHugh, K. J.; Jing, L.; Behrens, A. M.; Jayawardena, S.; Tang, W.; Gao, M.; Langer, R.; Jaklenec, A. Biocompatible Semiconductor Quantum Dots as Cancer Imaging Agents. *Adv. Mater.* **2018**, *30* (18), 1706356. DOI:10.1002/adma.201706356.

(21)    Zrazhevskiy, P.; Sena, M.; Gao, X. Designing Multifunctional Quantum Dots for Bioimaging, Detection, and Drug Delivery. *Chem. Soc. Rev.* **2010**, *39* (11), 4326–4354. DOI:10.1039/B915139G.

(22)    Liu, L.; Hu, R.; Law, W.-C.; Roy, I.; Zhu, J.; Ye, L.; Hu, S.; Zhang, X.; Yong, K.-T. Optimizing the Synthesis of Red- and near-Infrared $CuInS_2$ and $AgInS_2$ Semiconductor Nanocrystals for Bioimaging. *Analyst* **2013**, *138* (20), 6144–6153. DOI:10.1039/C3AN01030A.

(23)    Resch-Genger, U.; Grabolle, M.; Cavaliere-Jaricot, S.; Nitschke, R.; Nann, T. Quantum Dots versus Organic Dyes as Fluorescent Labels. *Nat. Methods* **2008**, *5* (9), 763–775. DOI:10.1038/nmeth.1248.

(24)    Das, A.; Snee, P. T. Synthetic Developments of Nontoxic Quantum Dots. *ChemPhysChem* **2016**, *17* (5), 598–617. DOI:10.1002/cphc.201500837.

(25)    Mughal, M. A.; Engelken, R.; Sharma, R. Progress in Indium (III) Sulfide ($In_2S_3$) Buffer Layer Deposition Techniques for CIS, CIGS, and CdTe-Based Thin Film Solar Cells. *Sol. Energy* **2015**, *120*, 131–146. DOI:10.1016/j.solener.2015.07.028.

(26)    Shen, S.; Wang, Q. Rational Tuning the Optical Properties of Metal Sulfide Nanocrystals and Their Applications. *Chem. Mater.* **2013**, *25* (8), 1166–1178. DOI:10.1021/cm302482d.

(27)    Xiong, W.-W.; Yang, G.-H.; Wu, X.-C.; Zhu, J.-J. Microwave-Assisted Synthesis of Highly Luminescent AgInS2/ZnS Nanocrystals for Dynamic Intracellular Cu(Ii) Detection. *J. Mater. Chem. B* **2013**, *1* (33), 4160–4165. DOI:10.1039/C3TB20638F.

(28)    Shamirian, A.; Appelbe, O.; Zhang, Q.; Ganesh, B.; Kron, S. J.; Snee, P. T. A Toolkit for Bioimaging Using Near-Infrared AgInS2/ZnS Quantum Dots. *J. Mater. Chem. B* **2015**, *3* (41), 8188–8196. DOI:10.1039/C5TB00247H.

(29)    Song, J.; Ma, C.; Zhang, W.; Yang, S.; Wang, S.; Lv, L.; Zhu, L.; Xia, R.; Xu, X. Tumor Cell-Targeted Zn3In2S6 and Ag–Zn–In–S Quantum Dots for Color Adjustable Luminophores. *J. Mater. Chem. B* **2016**, *4* (48), 7909–7918. DOI:10.1039/C6TB02297A.

(30)    Sheng, Y.; Tang, X.; Peng, E.; Xue, J. Graphene Oxide Based Fluorescent Nanocomposites for Cellular Imaging. *J. Mater. Chem. B* **2013**, *1* (4), 512–521. DOI:10.1039/C2TB00123C.

(31)    Zhao, P.; Zhang, J.; Zhu, Y.; Yang, X.; Jiang, X.; Yuan, Y.; Liu, C.; Li, C. A Novel Strategy for the Aqueous Synthesis of Down-/up-Conversion Nanocomposites for Dual-Modal Cell Imaging and Drug Delivery. *J. Mater. Chem. B* **2014**, *2* (47), 8372–8377. DOI:10.1039/C4TB01445F.

(32)    Moodelly, D.; Kowalik, P.; Bujak, P.; Pron, A.; Reiss, P. Synthesis, Photophysical Properties and Surface Chemistry of Chalcopyrite-Type Semiconductor Nanocrystals. *J. Mater. Chem. C* **2019**, *7* (38), 11665–11709. DOI:10.1039/C9TC03875B.

(33)    Mansur, A. A. P.; Mansur, H. S.; Tabare, C.; Paiva, A.; Capanema, N. S. V. Eco-Friendly AgInS$_2$/ZnS Quantum Dot Nanohybrids with Tunable Luminescent Properties Modulated by PH-Sensitive Biopolymer for Potential Solar Energy Harvesting Applications. *J. Mater. Sci. Mater. Electron.* **2019**, *30* (18), 16702–16717. DOI:10.1007/s10854-019-00719-0.

(34)    Hu, X.; Chen, T.; Xu, Y.; Wang, M.; Jiang, W.; Jiang, W. Hydrothermal Synthesis of Bright and Stable AgInS$_2$ Quantum Dots with Tunable Visible Emission. *J. Lumin.* **2018**, *200*, 189–195. DOI:10.1016/j.jlumin.2018.04.025.

(35)    Chang, J.-Y.; Wang, G.-Q.; Cheng, C.-Y.; Lin, W.-X.; Hsu, J.-C. Strategies for Photoluminescence Enhancement of AgInS$_2$ Quantum Dots and Their Application as Bioimaging Probes. *J. Mater. Chem.* **2012**, *22* (21), 10609–10618. DOI:10.1039/C2JM30679D.

(36)    Xiang, W.; Xie, C.; Wang, J.; Zhong, J.; Liang, X.; Yang, H.; Luo, L.; Chen, Z. Studies on Highly Luminescent AgInS$_2$ and Ag–Zn–In–S Quantum Dots. *J. Alloys Compd.* **2014**, *588*, 114–121.

DOI:10.1016/j.jallcom.2013.10.188.

(37)    Tian, L.; Elim, H. I.; Ji, W.; Vittal, J. J. One-Pot Synthesis and Third-Order Nonlinear Optical

Properties of AgInS$_2$ Nanocrystals. *Chem. Commun.* **2006**, No. 41, 4276–4278.

DOI:10.1039/B607855A.

(38)    Mansur, A. A. P.; Mansur, H. S.; Carvalho, S. M.; Caires, A. J. One-Pot Aqueous Synthesis of

Fluorescent Ag-In-Zn-S Quantum Dot/Polymer Bioconjugates for Multiplex Optical Bioimaging of

Glioblastoma Cells. *Contrast Media &#x26; Mol. Imaging* **2017**, *2017*, 3896107.

DOI:10.1155/2017/3896107.

(39)    Tan, L.; Liu, S.; Li, X.; Chronakis, I. S.; Shen, Y. A New Strategy for Synthesizing AgInS$_2$ Quantum

Dots Emitting Brightly in near-Infrared Window for in Vivo Imaging. *Colloids Surfaces B*

*Biointerfaces* **2015**, *125*, 222–229. DOI:10.1016/j.colsurfb.2014.11.041.

(40)    Zhou, J.; Yang, Y.; Zhang, C. Y. Toward Biocompatible Semiconductor Quantum Dots: From

Biosynthesis and Bioconjugation to Biomedical Application. *Chem. Rev.* **2015**, *115* (21), 11669–

11717. DOI:10.1021/acs.chemrev.5b00049.

(41)    Sakizadeh, J.; Cline, J. P.; Snyder, M. A.; Kiely, C. J.; McIntosh, S. Tailored Coupling of

Biomineralized CdS Quantum Dots to RGO to Realize Ambient Aqueous Synthesis of a High-

Performance Hydrogen Evolution Photocatalyst. *ACS Appl. Mater. Interfaces* **2020**, *12* (38), 42773–

42780. DOI:10.1021/acsami.0c11063.

(42)    Jiang, Z.; Wang, B.; Yu, J. C.; Wang, J.; An, T.; Zhao, H.; Li, H.; Yuan, S.; Wong, P. K.

AgInS$_2$/In$_2$S$_3$ Heterostructure Sensitization of Escherichia Coli for Sustainable Hydrogen

Production. *Nano Energy* **2018**, *46*, 234–240. DOI:10.1016/j.nanoen.2018.02.001.

(43)    Ozdemir, N. K.; Cline, J. P.; Kiely, C. J.; McIntosh, S.; Snyder, M. A. Scalable Biomineralization

of CdS Quantum Dots by Immobilized Cystathionine γ-Lyase. *ACS Sustain. Chem. Eng.* **2020**, *8*,

15189–15198. DOI:10.1021/acssuschemeng.0c04600.

(44)    Sadeghnejad, A.; Lu, L.; Cline, J.; Ozdemir, N. K.; Snyder, M. A.; Kiely, C. J.; McIntosh, S. In Situ

Biomineralization of Cu$_x$Zn$_y$Sn$_z$S$_4$ Nanocrystals within TiO$_2$-Based Quantum Dot Sensitized Solar

Cell Anodes. *ACS Appl. Mater. Interfaces* **2019**, *11* (49), 45656–45664. DOI:10.1021/acsami.9b15545.

(45)   Spangler, L. C.; Lu, L.; Kiely, C. J.; Berger, B. W.; McIntosh, S. Biomineralization of PbS and PbS-CdS Core-Shell Nanocrystals and Their Application in Quantum Dot Sensitized Solar Cells. *J. Mater. Chem. A* **2016**, *4* (16), 6107–6115. DOI:10.1039/c5ta10534j.

(46)   Spangler, L. C.; Chu, R.; Lu, L.; Kiely, C. J.; Berger, B. W.; McIntosh, S. Enzymatic Biomineralization of Biocompatible CuInS$_2$, (CuInZn)S$_2$ and CuInS$_2$/ZnS Core/Shell Nanocrystals for Bioimaging. *Nanoscale* **2017**, *9* (27), 9340–9351. DOI:10.1039/c7nr02852k.

(47)   Dunleavy, R.; Lu, L.; Kiely, C. J.; McIntosh, S.; Berger, B. W. Single-Enzyme Biomineralization of Cadmium Sulfide Nanocrystals with Controlled Optical Properties. *Proc. Natl. Acad. Sci. U. S. A.* **2016**, *113* (19), 5275–5280. DOI:10.1073/pnas.1523633113.

(48)   Chiku, T.; Padovani, D.; Zhu, W.; Singh, S.; Vitvitsky, V.; Banerjee, R. H$_2$S Biogenesis by Human Cystathionine γ-Lyase Leads to the Novel Sulfur Metabolites Lanthionine and Homolanthionine and Is Responsive to the Grade of Hyperhomocysteinemia. *J. Biol. Chem.* **2009**, *284* (17), 11601–11612. DOI:10.1074/jbc.M808026200.

(49)   Huang, S.; Li, H.; Ge, J. A Cardioprotective Insight of the Cystathionine γ-Lyase/Hydrogen Sulfide Pathway. *IJC Hear. Vasc.* **2015**, *7*, 51–57. DOI:10.1016/j.ijcha.2015.01.010.

(50)   De Trizio, L.; Manna, L. Forging Colloidal Nanostructures via Cation Exchange Reactions. *Chem. Rev.* **2016**, *116* (18), 10852–10887. DOI:10.1021/acs.chemrev.5b00739.

(51)   Cho, G.; Park, Y.; Hong, Y.-K.; Ha, D.-H. Ion Exchange: An Advanced Synthetic Method for Complex Nanoparticles. *Nano Converg.* **2019**, *6* (1), 17. DOI:10.1186/s40580-019-0187-0.

(52)   Rivest, J. B.; Jain, P. K. Cation Exchange on the Nanoscale: An Emerging Technique for New Material Synthesis, Device Fabrication, and Chemical Sensing. *Chem. Soc. Rev.* **2013**, *42* (1), 89–96. DOI:10.1039/C2CS35241A.

(53)   Pearson, R. G. Hard and Soft Acids and Bases. *J. Am. Chem. Soc.* **1963**, *85* (22), 3533–3539. DOI:10.1021/ja00905a001.

(54)    Yarema, O.; Yarema, M.; Wood, V. Tuning the Composition of Multicomponent Semiconductor Nanocrystals: The Case of I–III–VI Materials. *Chem. Mater.* **2018**, *30* (5), 1446–1461. DOI:10.1021/acs.chemmater.7b04710.

(55)    Xie, R.; Rutherford, M.; Peng, X. Formation of High-Quality I−III−VI Semiconductor Nanocrystals by Tuning Relative Reactivity of Cationic Precursors. *J. Am. Chem. Soc.* **2009**, *131* (15), 5691–5697. DOI:10.1021/ja9005767.

(56)    Doh, H.; Hwang, S.; Kim, S. Size-Tunable Synthesis of Nearly Monodisperse $Ag_2S$ Nanoparticles and Size-Dependent Fate of the Crystal Structures upon Cation Exchange to $AgInS_2$ Nanoparticles. *Chem. Mater.* **2016**, *28* (22), 8123–8127. DOI:10.1021/acs.chemmater.6b04011.

(57)    Shang, H.; Di, Q.; Ji, M.; Bai, B.; Liu, J.; Chen, W.; Xu, M.; Rong, H.; Liu, J.; Zhang, J. From Indium-Doped $Ag_2S$ to $AgInS_2$ Nanocrystals: Low-Temperature In Situ Conversion of Colloidal $Ag_2S$ Nanoparticles and Their NIR Fluorescence. *Chem. – A Eur. J.* **2018**, *24* (51), 13676–13680. DOI:10.1002/chem.201802973.

(58)    Kumta, P. N.; Phule, P. P.; Risbud, S. H. Low-Temperature Wet-Chemical Synthesis of Amorphous Indium Sulfide Powders. *Mater. Lett.* **1987**, *5* (10), 401–404. DOI:10.1016/0167-577X(87)90049-8.

(59)    Sumi, R.; Warrier, A. R.; Vijayan, C. Visible-Light Driven Photocatalytic Activity of β-Indium Sulfide ($In_2S_3$) Quantum Dots Embedded in Nafion Matrix. *J. Phys. D. Appl. Phys.* **2014**, *47* (10), 105103. DOI:10.1088/0022-3727/47/10/105103.

(60)    Sanz, C.; Guillén, C.; Gutiérrez, M. T.; Herrero, J. Investigation of Optical, Structural, and Chemical Properties of Indium Sulfide Thin Films Evaporated at Low Temperature by Modulated Flux Deposition. *Phys. Status Solidi* **2013**, *210* (2), 320–326. DOI:10.1002/pssa.201228259.

(61)    Gao, N.; Zhang, R.; Chen, B.; Zhang, J.; Zhang, X.; Rogach, A. L. Template Synthesis of Silver Indium Sulfide Based Nanocrystals Performed through Cation Exchange in Organic and Aqueous Media. *Nano Res.* **2020**, *14*, 2321–2329. DOI:10.1007/s12274-020-3229-3.

(62)    Li, X.; Tu, D.; Yu, S.; Song, X.; Lian, W.; Wei, J.; Shang, X.; Li, R.; Chen, X. Highly Efficient

Luminescent I-III-VI Semiconductor Nanoprobes Based on Template-Synthesized CuInS$_2$ Nanocrystals. *Nano Res.* **2019**, *12* (8), 1804–1809. DOI:10.1007/s12274-019-2435-3.

(63)    Nice, J. B.; Balashova, N. V; Kachlany, S. C.; Koufos, E.; Krueger, E.; Lally, E. T.; Brown, A. C. Aggregatibacter Actinomycetemcomitans Leukotoxin Is Delivered to Host Cells in an LFA-1-Indepdendent Manner When Associated with Outer Membrane Vesicles. *Toxins* **2018**, *10*, 414. DOI:10.3390/toxins10100414.

(64)    Zhou, G.; Liedmann, A.; Chatterjee, C.; Groth, T. In Vitro Study of the Host Responses to Model Biomaterials via a Fibroblast/Macrophage Co-Culture System. *Biomater. Sci.* **2017**, *5* (1), 141–152. DOI:10.1039/C6BM00247A.

(65)    Mir, I. A.; Radhakrishanan, V. S.; Rawat, K.; Prasad, T.; Bohidar, H. B. Bandgap Tunable AgInS Based Quantum Dots for High Contrast Cell Imaging with Enhanced Photodynamic and Antifungal Applications. *Sci. Rep.* **2018**, *8* (1), 9322. DOI:10.1038/s41598-018-27246-y.

(66)    Soares, J. X.; Wegner, K. D.; Ribeiro, D. S. M.; Melo, A.; Häusler, I.; Santos, J. L. M.; Resch-Genger, U. Rationally Designed Synthesis of Bright AgInS$_2$/ZnS Quantum Dots with Emission Control. *Nano Res.* **2020**, *13* (9), 2438–2450. DOI:10.1007/s12274-020-2876-8.

(67)    Babel, L.; Bonnet-Gómez, S.; Fromm, K. M. Appropriate Buffers for Studying the Bioinorganic Chemistry of Silver(I). *Chemistry* **2020**, *2*, 193–202. DOI:10.3390/chemistry2010012.

(68)    Leung, B. O.; Jalilehvand, F.; Mah, V.; Parvez, M.; Wu, Q. Silver(I) Complex Formation with Cysteine, Penicillamine, and Glutathione. *Inorg. Chem.* **2013**, *52* (8), 4593–4602. DOI:10.1021/ic400192c.

(69)    Yamagata, S.; Isaji, M.; Yamane, T.; Iwama, T. Substrate Inhibition of L-Cysteine α,β-Elimination Reaction Catalyzed by L-Cystathionine γ-Lyase of Saccharomyce Cerevisiae. *Biosci. Biotechnol. Biochem.* **2002**, *66* (12), 2706–2709. DOI:10.1271/bbb.66.2706.

(70)    Yu, S.-H.; Shu, L.; Wu, Y.-S.; Yang, J.; Xie, Y.; Qian, Y.-T. Organothermal Synthesis and Characterization of Nanocrystalline ß Indium Sulfide. *J. Am. Ceram. Soc.* **1999**, *82* (2), 457–460. DOI:10.1111/j.1551-2916.1999.tb20086.x.

(71)    Nosaka, Y.; Ohta, N.; Miyama, H. Photochemical Kinetics of Ultrasmall Semiconductor Particles in Solution: Effect of Size on the Quantum Yield of Electron Transfer. *J. Phys. Chem.* **1990**, *94* (9), 3752–3755. DOI:10.1021/j100372a073.

(72)    Raevskaya, A. E.; Ivanchenko, M. V; Stroyuk, O. L.; Kuchmiy, S. Y.; Plyusnin, V. F. Luminescent Ag-Doped In$_2$S$_3$ Nanoparticles Stabilized by Mercaptoacetate in Water and Glycerol. *J. Nanoparticle Res.* **2015**, *17* (3), 135. DOI:10.1007/s11051-015-2953-1.

(73)    Soni, V.; Raizada, P.; Kumar, A.; Hasija, V.; Singal, S.; Singh, P.; Hosseini-Bandegharaei, A.; Thakur, V. K.; Nguyen, V.-H. Indium Sulfide-Based Photocatalysts for Hydrogen Production and Water Cleaning: A Review. *Environ. Chem. Lett.* **2021**, *19*, 1065–1095. DOI:10.1007/s10311-020-01148-w.

(74)    Yamauchi, O.; Odani, A. Stability Constants of Metal Complexes of Amino Acids with Charged Side Chains - Part I: Positively Charged Side Chains. *Pure Appl. Chem.* **1996**, *68*, 469–496. DOI:10.1351/pac199668020469.

(75)    Su, D.; Wang, L.; Li, M.; Mei, S.; Wei, X.; Dai, H.; Hu, Z.; Xie, F.; Guo, R. Highly Luminescent Water-Soluble AgInS$_2$/ZnS Quantum Dots-Hydrogel Composites for Warm White LEDs. *J. Alloys Compd.* **2020**, *824*, 153896. DOI:10.1016/j.jallcom.2020.153896.

(76)    Gromova, Y.; Sokolova, A.; Kurshanov, D.; Korsakov, I.; Osipova, V.; Cherevkov, S.; Dubavik, A.; Maslov, V.; Perova, T.; Gun'ko, Y.; Baranov, A.; Fedorov, A. Investigation of AgInS$_2$/ZnS Quantum Dots by Magnetic Circular Dichroism Spectroscopy. *Materials* **2019**, *12*, 3616. DOI:10.3390/ma12213616.

(77)    Cai, C.; Zhai, L.; Ma, Y.; Zou, C.; Zhang, L.; Yang, Y.; Huang, S. Synthesis of AgInS$_2$ Quantum Dots with Tunable Photoluminescence for Sensitized Solar Cells. *J. Power Sources* **2017**, *341*, 11–18. DOI:10.1016/j.jpowsour.2016.11.101.

(78)    Dai, M.; Ogawa, S.; Kameyama, T.; Okazaki, K.; Kudo, A.; Kuwabata, S.; Tsuboi, Y.; Torimoto, T. Tunable Photoluminescence from the Visible to Near-Infrared Wavelength Region of Non-Stoichiometric AgInS$_2$ Nanoparticles. *J. Mater. Chem.* **2012**, *22* (25), 12851–12858.

DOI:10.1039/C2JM31463K.

(79)    Hong, S. P.; Park, H. K.; Oh, J. H.; Yang, H.; Do, Y. R. Comparisons of the Structural and Optical Properties of O-AgInS$_2$, t-AgInS$_2$, and c-AgIn$_5$S$_8$ Nanocrystals and Their Solid-Solution Nanocrystals with ZnS. *J. Mater. Chem.* **2012**, *22* (36), 18939–18949. DOI:10.1039/C2JM33879C.

(80)    Mrad, M.; Ben Chaabane, T.; Rinnert, H.; Lavinia, B.; Jasniewski, J.; Medjahdi, G.; Schneider, R. Aqueous Synthesis for Highly Emissive 3-Mercaptopropionic Acid-Capped AIZS Quantum Dots. *Inorg. Chem.* **2020**, *59* (9), 6220–6231. DOI:10.1021/acs.inorgchem.0c00347.

(81)    Shi, H.; Jia, L.; Wang, C.; Liu, E.; Ji, Z.; Fan, J. A High Sensitive and Selective Fluorescent Probe for Dopamine Detection Based on Water Soluble AgInS$_2$ Quantum Dots. *Opt. Mater.* **2020**, *99*, 109549. DOI:10.1016/j.optmat.2019.109549.

(82)    Hamanaka, Y.; Ozawa, K.; Kuzuya, T. Enhancement of Donor–Acceptor Pair Emissions in Colloidal AgInS$_2$ Quantum Dots with High Concentrations of Defects. *J. Phys. Chem. C* **2014**, *118* (26), 14562–14568. DOI:10.1021/jp501429f.

(83)    Hamanaka, Y.; Ogawa, T.; Tsuzuki, M.; Ozawa, K.; Kuzuya, T. Luminescence Properties of Chalcopyrite AgInS$_2$ Nanocrystals: Their Origin and Related Electronic States. *J. Lumin.* **2013**, *133*, 121–124. DOI:10.1016/j.jlumin.2011.10.006.

(84)    Kameyama, T.; Takahashi, T.; Machida, T.; Kamiya, Y.; Yamamoto, T.; Kuwabata, S.; Torimoto, T. Controlling the Electronic Energy Structure of ZnS–AgInS$_2$ Solid Solution Nanocrystals for Photoluminescence and Photocatalytic Hydrogen Evolution. *J. Phys. Chem. C* **2015**, *119* (44), 24740–24749. DOI:10.1021/acs.jpcc.5b07994.

(85)    Lakowicz, J. R. Principles of Fluorescence Spectroscopy; Springer: New York, 2006; pp 97–101.

(86)    Lv, J.; Liang, X. Tunable Photoluminescence of Cd Free AgInS$_2$ Quantum Dots: Synthesis and Application for Light Emitting Diodes. *Opt. Mater.* **2017**, *72*, 805–808. DOI:10.1016/j.optmat.2017.07.028.

(87)    Murray, C. B.; Norris, D. J.; Bawendi, M. G. Synthesis and Characterization of Nearly Monodisperse CdE (E = Sulfur, Selenium, Tellurium) Semiconductor Nanocrystallites. *J. Am.*

*Chem. Soc.* **1993**, *115* (19), 8706–8715. DOI:10.1021/ja00072a025.

(88)   Torimoto, T.; Ogawa, S.; Adachi, T.; Kameyama, T.; Okazaki, K.; Shibayama, T.; Kudo, A.; Kuwabata, S. Remarkable Photoluminescence Enhancement of ZnS–AgInS₂ Solid Solution Nanoparticles by Post-Synthesis Treatment. *Chem. Commun.* **2010**, *46* (12), 2082–2084. DOI:10.1039/B924186H.

(89)   Jiang, P.; Zhu, C.-N.; Zhu, D.-L.; Zhang, Z.-L.; Zhang, G.-J.; Pang, D.-W. A Room-Temperature Method for Coating a ZnS Shell on Semiconductor Quantum Dots. *J. Mater. Chem. C* **2015**, *3* (5), 964–967. DOI:10.1039/C4TC02437K.

(90)   Delices, A.; Moodelly, D.; Hurot, C.; Hou, Y.; Ling, W. L.; Saint-Pierre, C.; Gasparutto, D.; Nogues, G.; Reiss, P.; Kheng, K. Aqueous Synthesis of DNA-Functionalized Near-Infrared AgInS₂/ZnS Core/Shell Quantum Dots. *ACS Appl. Mater. Interfaces* **2020**, *12* (39), 44026–44038. DOI:10.1021/acsami.0c11337.

(91)   Xu, G.; Zeng, S.; Zhang, B.; Swihart, M. T.; Yong, K.-T.; Prasad, P. N. New Generation Cadmium-Free Quantum Dots for Biophotonics and Nanomedicine. *Chem. Rev.* **2016**, *116* (19), 12234–12327. DOI:10.1021/acs.chemrev.6b00290.

(92)   Strober, W. Trypan Blue Exclusion Test of Cell Viability. *Curr. Protoc. Immunol.* **2015**, *111* (1), A3.B.1-A3.B.3. DOI:10.1002/0471142735.ima03bs111.

(93)   Bradburne, C. E.; Delehanty, J. B.; Boeneman Gemmill, K.; Mei, B. C.; Mattoussi, H.; Susumu, K.; Blanco-Canosa, J. B.; Dawson, P. E.; Medintz, I. L. Cytotoxicity of Quantum Dots Used for In Vitro Cellular Labeling: Role of QD Surface Ligand, Delivery Modality, Cell Type, and Direct Comparison to Organic Fluorophores. *Bioconjug. Chem.* **2013**, *24* (9), 1570–1583. DOI:10.1021/bc4001917.

(94)   Oluwafemi, O. S.; May, B. M. M.; Parani, S.; Rajendran, J. V. Cell Viability Assessments of Green Synthesized Water-Soluble AgInS₂/ZnS Core/Shell Quantum Dots against Different Cancer Cell Lines. *J. Mater. Res.* **2019**, *34* (24), 4037–4044. DOI:10.1557/jmr.2019.362.

(95)   Starr, T.; Bauler, T. J.; Malik-Kale, P.; Steele-Mortimer, O. The Phorbol 12-Myristate-13-Acetate

Differentiation Protocol Is Critical to the Interaction of THP-1 Macrophages with Salmonella Typhimurium. *PLoS One* **2018**, *13* (3), e0193601–e0193601. DOI:10.1371/journal.pone.0193601.

(96)    Park, E. K.; Jung, H. S.; Yang, H. I.; Yoo, M. C.; Kim, C.; Kim, K. S. Optimized THP-1 Differentiation Is Required for the Detection of Responses to Weak Stimuli. *Inflamm. Res.* **2007**, *56* (1), 45–50. DOI:10.1007/s00011-007-6115-5.

(97)    Downey, G. P.; Doherty, D. E.; Schwab, B.; Elson, E. L.; Henson, P. M.; Worthen, G. S. Retention of Leukocytes in Capillaries: Role of Cell Size and Deformability. *J. Appl. Physiol.* **1990**, *69* (5), 1767–1778. DOI:10.1152/jappl.1990.69.5.1767.

(98)    Guertin, D. A.; Sabatini, D. M. Cell Size Control. *eLS*. January 27, 2006. DOI:10.1038/npg.els.0003359.

(99)    Christensen, J. E.; Andreasen, S. Ø.; Christensen, J. P.; Thomsen, A. R. CD11b Expression as a Marker to Distinguish between Recently Activated Effector CD8+ T Cells and Memory Cells. *Int. Immunol.* **2001**, *13* (4), 593–600. DOI:10.1093/intimm/13.4.593.